

1 TUNGSTEN ISOTOPIC COMPOSITIONS IN STARDUST SiC GRAINS  
2 FROM THE MURCHISON METEORITE: CONSTRAINTS ON THE *s*-  
3 PROCESS IN THE Hf-Ta-W-Re-Os REGION

4 JANAÍNA N. ÁVILA <sup>1,2,3</sup>, MARIA LUGARO <sup>4</sup>, TREVOR R. IRELAND <sup>1,2</sup>, FRANK GYNGARD <sup>5</sup>,  
5 ERNST ZINNER <sup>5</sup>, SERGIO CRISTALLO <sup>6,7</sup>, PETER HOLDEN <sup>1</sup>, JOELENE BUNTAIN <sup>4</sup>,  
6 SACHIKO AMARI <sup>5</sup>, AND AMANDA KARAKAS <sup>8</sup>

7  
8  
9 <sup>1</sup> Research School of Earth Sciences, The Australian National University, Canberra ACT 0200,  
10 Australia; janaina.avila@anu.edu.au

11 <sup>2</sup> Planetary Science Institute, The Australian National University, Canberra ACT 0200, Australia

12 <sup>3</sup> Current address: Astronomy Department/IAG, University of São Paulo, São Paulo SP 05508-090,  
13 Brazil

14 <sup>4</sup> Centre for Stellar and Planetary Astrophysics, Monash University, Clayton VIC 3800, Australia

15 <sup>5</sup> Laboratory for Space Sciences and the Department of Physics, Washington University, One  
16 Brookings Drive, St. Louis, MO 63130, USA

17 <sup>6</sup> Departamento de Física Teórica y del Cosmos, Universidad de Granada, Granada 18071, Spain

18 <sup>7</sup> Current address: Osservatorio Astronomico di Collurania, INAF, Teramo 64100, Italy

19 <sup>8</sup> Mount Stromlo Observatory, Australian National University, Weston Creek ACT 2611, Australia

20  
21 *The Astrophysical Journal*

22  
23 Short Title:

24 W ISOTOPIC COMPOSITIONS IN STARDUST SiC GRAINS

25

ABSTRACT

26  
27  
28  
29  
30  
31  
32  
33  
34  
35  
36  
37  
38  
39  
40  
41  
42  
43  
44  
45  
46  
47  
48

We report the first tungsten isotopic measurements in stardust silicon carbide (SiC) grains recovered from the Murchison carbonaceous chondrite. The isotopes  $^{182,183,184,186}\text{W}$  and  $^{179,180}\text{Hf}$  were measured on both an aggregate (KJB fraction) and single stardust SiC grains (LS+LU fraction) believed to have condensed in the outflows of low-mass carbon-rich asymptotic giant branch (AGB) stars with close-to-solar metallicity. The SiC aggregate shows small deviations from terrestrial (=solar) composition in the  $^{182}\text{W}/^{184}\text{W}$  and  $^{183}\text{W}/^{184}\text{W}$  ratios, with deficits in  $^{182}\text{W}$  and  $^{183}\text{W}$  with respect to  $^{184}\text{W}$ . The  $^{186}\text{W}/^{184}\text{W}$  ratio, however, shows no apparent deviation from the solar value. Tungsten isotopic measurements in single mainstream stardust SiC grains revealed lower than solar  $^{182}\text{W}/^{184}\text{W}$ ,  $^{183}\text{W}/^{184}\text{W}$ , and  $^{186}\text{W}/^{184}\text{W}$  ratios. We have compared the SiC data with theoretical predictions of the evolution of W isotopic ratios in the envelopes of AGB stars. These ratios are affected by the slow neutron-capture process and match the SiC data regarding their  $^{182}\text{W}/^{184}\text{W}$ ,  $^{183}\text{W}/^{184}\text{W}$ , and  $^{179}\text{Hf}/^{180}\text{Hf}$  isotopic compositions, although a small adjustment in the *s*-process production of  $^{183}\text{W}$  is needed in order to have a better agreement between the SiC data and model predictions. The models cannot explain the  $^{186}\text{W}/^{184}\text{W}$  ratios observed in the SiC grains, even when the current  $^{185}\text{W}$  neutron-capture cross section is increased by a factor of two. Further study is required to better assess how model uncertainties (e.g., the formation of the  $^{13}\text{C}$  neutron source, the mass-loss law, the modelling of the third dredge-up, and the efficiency of the  $^{22}\text{Ne}$  neutron source) may affect current *s*-process predictions.

*Subject headings:* dust, extinction — nuclear reactions, nucleosynthesis, abundances — stars: AGB and post-AGB — stars: carbon

## 1. INTRODUCTION

49

50 Stardust grains condensed directly from the gas phase present in ancient stellar outflows or  
51 stellar ejecta, and thus became part of the interstellar medium from which our Solar System  
52 formed about 4.57 Gyr ago. Their stellar origins are indicated by unusual isotopic  
53 compositions (essentially for every element) relative to those found in Solar System materials  
54 (i.e., terrestrial, lunar, and meteoritic samples). The deviations from the recommended Solar  
55 System isotopic abundances, which are taken from compilations of isotopic measurements of  
56 terrestrial materials except for H and the noble gases (e.g., Anders & Grevesse 1989; Lodders  
57 2003, 2010), are too large to be explained by mass-fractionation processes or by decay of  
58 longer-lived radioactive isotopes. Instead, the observed isotopic compositions can only be  
59 explained by nucleosynthetic processes (see reviews by Zinner, 1998, 2004; Clayton and  
60 Nittler, 2004; Lodders and Amari, 2005).

61 Isotopic compositions of several heavy elements have been measured in stardust grains  
62 believed to have condensed in the outflows of low-mass carbon-rich asymptotic giant branch  
63 (AGB) stars (e.g., Zr, Nicolussi et al. 1997; Mo, Nicolussi et al. 1998a; Sr, Nicolussi et al.  
64 1998b; Ba, Savina et al. 2003; Ru, Savina et al. 2004). The grain data have provided detailed  
65 information on the nucleosynthesis of heavy elements produced by the slow neutron capture  
66 process (the *s*-process). However, the available data are still scarce or no data exist for some  
67 heavy elements. One of the main gaps involves nuclides in the Hf-Ta-W-Re-Os region.

68 The *s*-process path in the Hf-Ta-W-Re-Os region (Fig. 1) has recently received considerable  
69 attention. New experimental data (neutron-capture reaction rates) for Hf, W, and Os nuclides  
70 have been reported (Sonnabend et al. 2003; Mohr et al. 2004; Mosconi et al. 2006, 2010a,b;  
71 Wisshak et al. 2006; Segawa et al. 2007; Vockenhuber et al. 2007; Marganiec et al. 2009;

72 Fujii et al. 2010), and small anomalies of nucleosynthetic origin in W and Os isotopes have  
73 been observed in primitive meteorites (Brandon et al. 2005; Yokoyama et al. 2007, 2011; Qin  
74 et al. 2008; Reisberg et al. 2009). Recent *s*-process analyses of the Hf-Ta-W-Re-Os region  
75 have identified two major problems. First, it appears that model predictions underestimate the  
76 *s*-process contribution to the  $^{182}\text{W}$  solar abundance and, consequently, the  $^{182}\text{W}$  *r*-residual  
77 (obtained by subtracting the calculated *s*-process from the observed Solar System abundance)  
78 shows a significant positive deviation from the otherwise very smooth rapid neutron-capture  
79 process (the *r*-process) solar abundance pattern (see Fig. 12 of Wisshak et al. 2006; and Fig. 6  
80 of Vockenhuber et al. 2007). Second, an analysis of the *s*-process flow at the  $^{185}\text{W}$  branching  
81 point shows that the predicted  $^{186}\text{Os}$  *s*-process abundance is also somewhat problematic,  
82 suggesting a significant overproduction ( $\sim 20\%$ ) with respect to its solar abundance  
83 (Sonnabend et al. 2003). This is not allowed, theoretically, because  $^{186}\text{Os}$  is an *s*-only isotope,  
84 being shielded by the stable  $^{186}\text{W}$  from the chain of radioactive decays that follow the *r*-  
85 process. In line with this, isotopic anomalies of nucleosynthetic origin found in Os isotopes  
86 measured in primitive meteorites suggest a lower  $^{186}\text{Os}/^{188}\text{Os}$  *s*-process ratio than current  
87 models predict (Brandon et al. 2005; Yokoyama et al. 2007). The problematic  $^{182}\text{W}$  and  $^{186}\text{Os}$   
88 *s*-process abundances and, consequently, the inferred  $^{182}\text{W}$  *r*-residual, may reflect remaining  
89 uncertainties related to the experimental cross section data and the current *s*-process models.

90 Tungsten has five stable isotopes: the rare  $^{180}\text{W}$  (0.12% of solar W), which is mainly produced  
91 by proton-capture or photodisintegration processes (*p*-process), and  $^{182}\text{W}$  (26.5%),  $^{183}\text{W}$   
92 (14.3%),  $^{184}\text{W}$  (30.6%), and  $^{186}\text{W}$  (28.4%), which are of mixed *s*- and *r*-process origin. As  
93 illustrated in Figure 1, the branchings at  $^{181,182}\text{Hf}$  and  $^{182,183}\text{Ta}$  may affect the W *s*-process  
94 isotopic pattern, and the branching at  $^{185}\text{W}$  determines the  $^{186}\text{W}$  abundance and may affect the  
95 Re and Os isotopic patterns.

96 Here we report the results of the first W isotopic analyses performed on five large stardust  
97 SiC grains (LS+LU fraction) extracted from the Murchison carbonaceous chondrite (Amari et  
98 al. 1994). In addition to the individual grains, we also analysed a SiC-enriched bulk sample  
99 (KJB fraction, Amari et al. 1994). Carbon-, N-, and Si-isotopic ratios for the KJB fraction and  
100 individual SiC grains from the LS+LU fraction have been previously reported by Amari et al.  
101 (2000) and Virag et al. (1992), and are reproduced in Figure 2 and Table 1. The mount  
102 containing grains from the LS+LU fraction used in this study is the same previously  
103 investigated by Virag et al. (1992) and Ireland et al. (1991). Virag et al. (1992) have shown  
104 that SiC grains from the LS+LU fraction contain several unique features: some are very large  
105 (over 20  $\mu\text{m}$ ); many of these large grains appear to have flat and smooth surfaces, unlike the  
106 euhedral surfaces observed in smaller grains; and isotopic compositions show clustering for C  
107 and Si and even for Ti (Ireland et al. 1991). Recent studies have shown that stardust SiC  
108 grains from the LS+LU fraction have interstellar exposure ages ranging from  $\sim 3$  Myr to  $\sim 1$   
109 Gyr (Gyngard et al., 2009a, 2009b; Heck et al., 2009), which implies that the parent stars of  
110 the grains must have ended their lives within this time range before the formation of the Solar  
111 System. Based on their C-, N-, and Si-isotopic compositions, the five single SiC grains  
112 analysed for W are classified as “mainstream grains”, and are interpreted to have condensed  
113 in the outflows of low-mass ( $\sim 1.5$  to  $3 M_{\odot}$ ), carbon-rich AGB stars with close-to-solar  
114 metallicity (Hoppe et al. 1994; Zinner et al. 2006). The KJB fraction also shows C-, N-, and  
115 Si-isotopic signatures consistent with an AGB origin for most of the grains (Amari et al.  
116 2000).

117

118

## 2. TUNGSTEN ISOTOPIC MEASUREMENTS

119

120 While  $^{182}\text{W}$  and  $^{183}\text{W}$  are free of interferences, the remaining W isotopes have atomic isobaric  
121 interferences:  $^{180}\text{W}$  from  $^{180}\text{Ta}^+$  (0.012% of solar Ta) and  $^{180}\text{Hf}^+$  (35.1% of solar Hf),  $^{184}\text{W}$  from  
122  $^{184}\text{Os}^+$  (0.02% of solar Os), and  $^{186}\text{W}$  from  $^{186}\text{Os}^+$  (1.59% of solar Os). Monoxide interferences  
123 are also present (e.g.  $^{170}\text{Er}^{16}\text{O}^+$  and  $^{170}\text{Yb}^{16}\text{O}^+$  on  $^{186}\text{W}^+$ ), requiring a mass resolution of  $m/\Delta m \sim$   
124 8000 for separation. Detailed scans in the mass region of  $\text{W}^+$  and  $\text{WO}^+$  isotopic species,  
125 sputtered from NIST-610 silicate glass and a SiC ceramic doped with heavy elements, have  
126 shown that  $\text{WO}^+$  species are produced at a higher intensity than  $\text{W}^+$  species during sputtering  
127 by a 10 keV  $\text{O}_2^-$  primary ion beam ( $\text{WO}^+/\text{W}^+ \sim 3$ ). Furthermore, as previously described by  
128 Kinny et al. (1991), under the same analytical conditions  $\text{YbO}^+/\text{Yb}^+ \sim 0.5$ , and  
129  $\text{REEO}_2^+/\text{REEO}^+$  is negligible ( $< 0.001$ ). Analysing  $\text{WO}^+$  instead of  $\text{W}^+$  therefore produces  
130 higher yields and minimises interferences from  $\text{REE}^+$ ,  $\text{REEO}^+$ , and  $\text{REEO}_2^+$  species. For these  
131 reasons we analysed W isotopes as  $\text{WO}^+$ .

132 Tungsten isotopic measurements in stardust SiC grains were carried out with a Sensitive High  
133 Resolution Ion Microprobe – Reverse Geometry (SHRIMP-RG) at the Australian National  
134 University. We performed both “bulk analyses” on an aggregate of many grains from the KJB  
135 fraction and “single-grain analyses” on grains from the LS+LU fraction. Nine individual spots  
136 on the KJB fraction were analysed for W isotopes. Five out of nine investigated single grains  
137 from the LS+LU fraction had sufficiently high W concentrations for isotopic analysis.  
138 SHRIMP-RG measurements were performed with an  $\text{O}_2^-$  primary beam of  $\sim 5$  nA focused to  
139 sputter an area of  $\sim 30$   $\mu\text{m}$  in diameter. Before data acquisition, each spot/grain was initially  
140 rastered across an area slightly larger than the analytical pit by the beam for  $\sim 60$  s to  
141 minimise surface contamination. Secondary ions were extracted at 10 kV and measured by  
142 single collector analysis on an ETP<sup>TM</sup> multiplier in peak-jumping mode.

143 We used two different setups. In the first setup (KJB spots #01 – 08), we measured  $^{180}\text{Hf}^{16}\text{O}^+$ ,  
144  $^{182}\text{W}^{16}\text{O}^+$ ,  $^{183}\text{W}^{16}\text{O}^+$ ,  $^{184}\text{W}^{16}\text{O}^+$ ,  $^{186}\text{W}^{16}\text{O}^+$ ,  $^{188}\text{Os}^{16}\text{O}^+$ , and  $^{189}\text{Os}^{16}\text{O}^+$ . We monitored  $\text{OsO}^+$  in order  
145 to estimate a potential interference on the  $^{186}\text{W}^{16}\text{O}^+$  peak. However, no contribution was found  
146 in the mass regions of  $^{188}\text{Os}^{16}\text{O}^+$  and  $^{189}\text{Os}^{16}\text{O}^+$ . In the second setup (KJB spot # 09, and all  
147 individual grains), we measured  $^{179}\text{Hf}^{16}\text{O}^+$ ,  $^{180}\text{Hf}^{16}\text{O}^+$ ,  $^{182}\text{W}^{16}\text{O}^+$ ,  $^{183}\text{W}^{16}\text{O}^+$ ,  $^{184}\text{W}^{16}\text{O}^+$ ,  $^{186}\text{W}^{16}\text{O}^+$ ,  
148  $^{188}\text{Os}^{16}\text{O}^+$ , and  $^{189}\text{Os}^{16}\text{O}^+$ . Contributions from  $^{180}\text{W}^{16}\text{O}^+$  on the  $^{180}\text{Hf}^{16}\text{O}^+$  peak,  $^{180}\text{Hf}^{18}\text{O}^+$  on the  
149  $^{182}\text{W}^{16}\text{O}^+$  peak, and  $^{182}\text{W}^{18}\text{O}^+$  on the  $^{184}\text{W}^{16}\text{O}^+$  peak were found to be negligible, so no  
150 correction was applied. In addition, we carefully checked the mass region of interest for  
151 molecular interferences (Fig. 3) resulting from complex combinations of major elements from  
152 the SiC matrix. Low count rates (e.g.,  $\sim 0.4$  counts/s at mass 198) were found in the mass  
153 region of interest when sputtering a “pure” synthetic SiC. Count rates at mass 198 sputtered  
154 from the KJB fraction are usually in the order of 20 counts/s. Individual grains, on the other  
155 hand, had count rates between 1.5 and 8 counts/s. The use of a small energy offset ( $\sim 21\text{-}24$   
156 eV) has proved to be quite successful in suppressing complex molecular interferences without  
157 significantly compromising the intensity of the atomic species (Ávila et al. 2011, in  
158 preparation). In this study, we confirmed this observation for the mass region of interest using  
159 a “pure” synthetic SiC reference material. As a result, W (and also Hf) measurements in all  
160 individual SiC grains and 5 out of 11 KJB spots (#07 – 11) were carried out on the SHRIMP-  
161 RG by combining high-mass resolution with energy filtering. Six KJB spots (#01 – 06) were  
162 analysed without energy filtering. We found that all KJB spots have the same W isotopic  
163 composition within 2 sigma errors. KJB spots # 10 and 11 were analysed only for  $^{179}\text{Hf}/^{180}\text{Hf}$   
164 ratios.

165 The acquisition time for each analysis was  $\sim 6\text{-}7$  min. Because of the low W abundance in  
166 stardust SiC grains, the mass positions of  $\text{WO}^+$  isotopic species could not be monitored during

167 each individual analysis. Their mass positions were instead maintained from the previous  
168 measurement on the standard. We systematically bracketed three unknowns by a suite of  
169 standard reference materials (i.e., NIST-610 silicate glass and SiC ceramic). The shifts in  
170 peak positions monitored during the analytical sessions were found to be less than 0.002  
171 a.m.u. between consecutive standards. The secondary beam was aligned using the QQH  
172 monitor, allowing maximum transmission through the source slit. SHRIMP-RG was operated  
173 at a mass resolution of  $m/\Delta m = 7000$  (at 10% peak). The NIST-610 silicate glass and the SiC  
174 ceramic doped with heavy elements were used to monitor instrumental mass fractionation  
175 (IMF). The data were corrected for an IMF of  $-12\text{‰}$   $\text{amu}^{-1}$  based on the  $^{186}\text{W}/^{183}\text{W}$  ratio of  
176 1.986 (Jacobsen 2005), and the mean of the  $^{186}\text{W}/^{183}\text{W}$  measurements of the SiC standards.  
177 Mass interferences and background were monitored by periodically analysing a “pure”  
178 synthetic SiC and the Au foil (i.e., the substrate on which the grains were deposited). The  
179  $^{180}\text{Hf}/^{184}\text{W}$  ratios were normalized by applying the relative sensitivity factor (RSF) determined  
180 by measuring the SiC ceramic doped with heavy elements.

181 The isotopic ratios obtained with SHRIMP-RG in single-collection mode were calculated  
182 using Dodson's time-interpolation algorithm (Dodson 1978) (Table 2), wherein the final  
183 isotopic ratios are calculated as means of  $N-1$  interpolated ratios ( $N =$  number of scans). To  
184 investigate the hypothesis that the isotopic measurements calculated using this approach could  
185 be affected by a systematic positive bias, we also calculated the isotopic ratios from the total  
186 counts as suggested by Huss et al. (2011) and Ogliore et al. (2011). We found slight  
187 differences ( $< 5\%$ ) in the final ratios, but all are well within the errors. The uncertainties of  
188 the W and Hf isotopic ratios measured on stardust SiC grains are dominated by counting  
189 statistics, and were calculated from the standard deviation of the sampling distribution (i.e.  
190 standard error =  $\text{S.D.}/\sqrt{n}$ ). Uncertainties related to the dispersion (i.e. standard deviation) of

191 measurements on the standards during the analytical session were calculated from repeated  
192 analysis of NIST-610 and SiC ceramic, and propagated into the uncertainty of each unknown.

193

194

### 3. RESULTS

195 Tungsten and hafnium isotopic compositions are reported in Table 2. The quoted errors are  
196  $\pm 1\sigma$ . The reference W isotopic composition is taken from Jacobsen (2005). This composition  
197 is taken as a terrestrial composition that should also reflect the Solar System composition  
198 (e.g., Lodders 2010), which is the case for most refractory elements. Isotope compositions are  
199 either reported directly or as delta ( $\delta$ ) values, defined as  $\delta R = [(R_{\text{measured}}/R_{\text{solar}} - 1) \times 1000]$ ,  
200 where the measured isotopic ratios ( $R_{\text{measured}}$ ) are expressed as deviations from the reference  
201 terrestrial (=solar) isotopic composition ( $R_{\text{solar}}$ ) in parts per thousand (‰). Other interelement  
202 isotopic ratios are taken from Lodders (2010).

203 The weighted mean W isotopic ratios obtained for the SiC-enriched bulk sample (KJB  
204 fraction), based on 9 measurements (Table 2 and Fig. 4), are  $^{182}\text{W}/^{184}\text{W} = 0.809 \pm 0.014$   
205 ( $\delta^{182}\text{W}/^{184}\text{W} = -64 \pm 17 \text{‰}$ ),  $^{183}\text{W}/^{184}\text{W} = 0.411 \pm 0.009$  ( $\delta^{183}\text{W}/^{184}\text{W} = -120 \pm 22 \text{‰}$ ), and  
206  $^{186}\text{W}/^{184}\text{W} = 0.944 \pm 0.024$  ( $\delta^{186}\text{W}/^{184}\text{W} = 18 \pm 26 \text{‰}$ ). The KJB fraction shows a small  
207 deviation from solar composition in both  $^{182}\text{W}/^{184}\text{W}$  and  $^{183}\text{W}/^{184}\text{W}$  ratios, with deficits in  $^{182}\text{W}$   
208 and  $^{183}\text{W}$  with respect to  $^{184}\text{W}$ . The  $^{186}\text{W}/^{184}\text{W}$  ratio, however, shows no apparent deviation  
209 from the solar value, which raises the possibility of contamination with solar material.  
210 Although contamination is possible, we believe it is unlikely since the other ratios (e.g.,  
211  $^{182}\text{W}/^{184}\text{W}$  and  $^{183}\text{W}/^{184}\text{W}$ ) are statistically anomalous.

212 Within the  $\pm 1\sigma$  uncertainties, the W isotopic ratios determined for two out of five single  
213 grains (LU-34 and LU-32) show no deviation from solar composition. On the other hand, two  
214 other grains (LU-36 and LU-41) exhibit deficits in  $^{182}\text{W}$ ,  $^{183}\text{W}$ , and  $^{186}\text{W}$  with respect to  $^{184}\text{W}$ .  
215 Grain LU-20 shows a deviation from the solar value only in the  $^{186}\text{W}/^{184}\text{W}$  ratio, with both  
216  $^{182}\text{W}/^{184}\text{W}$  and  $^{183}\text{W}/^{184}\text{W}$  ratios showing no apparent deviation from solar within errors. Only  
217 grain LU-41 has deviations from the solar isotopic ratios that are larger than  $2\sigma$ . No obvious  
218 correlations between W isotopic compositions and C-, N-, and Si-isotopic compositions were  
219 found.

220 Additionally, we provide information on the  $^{179}\text{Hf}/^{180}\text{Hf}$  ratios (Table 2). The weighted mean  
221  $^{179}\text{Hf}/^{180}\text{Hf}$  of the SiC-enriched bulk sample (KJB fraction), based on 3 measurements, is  
222  $0.326 \pm 0.033$  ( $\delta^{179}\text{Hf}/^{180}\text{Hf} = -160 \pm 85 \text{‰}$ ). This value deviates only slightly from that  
223 reported for the Solar System ( $^{179}\text{Hf}/^{180}\text{Hf} = 0.388$ ; Lodders 2010). Three out of five  
224 investigated single grains had sufficiently high Hf concentrations for isotopic analysis. Two  
225 of them show no apparent deviation from the solar value (within  $1\sigma$  error). Grain LU-41,  
226 which has the largest deficit in  $^{182}\text{W}$ ,  $^{183}\text{W}$ , and  $^{186}\text{W}$  with respect to  $^{184}\text{W}$ , also has a significant  
227 deficit in  $^{179}\text{Hf}$  with respect to  $^{180}\text{Hf}$  ( $\delta^{179}\text{Hf}/^{180}\text{Hf} = -637 \pm 121 \text{‰}$ ). All single grains and KJB  
228 spot analyses show lower  $^{180}\text{Hf}/^{184}\text{W}$  ratios than current predictions from *s*-process  
229 nucleosynthesis calculations (see section 4).

230 We shall now consider some factors that may affect the present determinations. First, there is  
231 a potential problem of contamination with foreign materials and minerals, originating either  
232 from the meteorite itself or as a result of sample preparation. Tungsten, unfortunately, may be  
233 a contaminant from the sample preparation. Sodium polytungstate was used for density  
234 separation of graphite from SiC (Amari et al. 1994). The density separation was followed by  
235 several washing procedures in order to remove any contaminants. Based on the behaviour of

236 the isotopic ratios as a function of acquisition time, there is no evidence from our analyses to  
237 suggest that the W isotopic compositions are not intrinsic to the grains or result from surface  
238 contamination. Furthermore, we did not detect W in the Au-foil, onto which both the KJB and  
239 LS+LU fractions had been deposited. Nonetheless, three out of five single grains show no  
240 apparent deviation from the solar isotopic ratios (for both W and Hf), and contamination with  
241 solar material cannot be completely ruled out. Kashiv (2004) found very high W abundance in  
242 stardust SiC grains (W enrichment factor, relative to solar W/Si ratio, of  $\sim 300$  to 8700), much  
243 higher than expected based on AGB stellar models and thermodynamic condensation  
244 calculations. In contrast to Kashiv (2004), our W concentration measurements are semi-  
245 quantitative only. Nevertheless, we found for the KJB fraction a W enrichment factor  $\sim 10$ ,  
246 and for the single grains from the LS+LU fraction an enrichment factor  $< 3$ , which are much  
247 lower than the values found by Kashiv (2004). This author also suggested that W  
248 contamination could be from heavy metal alloy holders used during analytical procedures.  
249 Contamination from the Murchison meteorite is another possibility. In order to minimize any  
250 residual surface contamination, all spots and grains analysed were initially rastered across an  
251 area slightly larger than the analytical pit by the  $O_2^-$  primary beam for  $\sim 60$  s before data  
252 acquisition.

253 Another complication encountered during ion microprobe analysis of SiC grains is the lack of  
254 suitable SiC standards. The accuracy and precision of ion microprobe measurements is known  
255 to be highly dependent on the availability of suitable standards because of the variability of  
256 ion emission produced by sputtering of solid geological and cosmochemical materials.  
257 Standards that are compositionally and structurally similar to the analytical target, i.e., matrix-  
258 matched, are therefore highly desirable. Furthermore, assessment of molecular interferences  
259 produced by combinations of isotopes of the major elements is particularly important for the

260 analysis of trace elements where even weak molecular interferences may significantly  
261 contribute to the mass peak being measured. Naturally occurring (except for stardust SiC  
262 grains) and synthetic SiC samples contain very low abundances of trace elements and are  
263 therefore not suitable as standard materials. While the synthesis of large doped SiC crystals in  
264 the laboratory is extremely difficult, SiC-based ceramics sintered with desirable amounts of  
265 trace elements are relatively easy to produce. In order to determine elemental yields and  
266 identify possible molecular interferences in the mass region of W isotopes, we prepared a SiC  
267 ceramic doped with several trace elements at nominal concentrations between 1 and 3000  
268 ppm. The SiC ceramic has proved to be a useful standard for elemental and isotopic  
269 measurements in stardust SiC grains, especially concerning identification of molecular  
270 interferences.

271

#### 272 4. W AND Hf CONDENSATION INTO SiC GRAINS FROM AGB STARS

273 The  $^{180}\text{Hf}/^{184}\text{W}$  ratios obtained here for stardust SiC grains (0.041 to 0.276) are lower than *s*-  
274 process model predictions for the envelope compositions of carbon-rich, low-mass AGB stars  
275 with close-to-solar metallicity ( $\sim 1.42$ <sup>1</sup>; Solar System  $\sim 1.30$ , Lodders 2010). Clearly, it is not  
276 possible to attribute the observed range to nucleosynthetic effects or to contamination with  
277 solar material. Hence, we turn to discussing the condensation behaviour of W and Hf to see if  
278 this could provide an explanation. According to Lodders & Fegley (1995), under the same  
279 conditions of pressure and C/O ratio, W condenses as WC at a temperature  $\sim 100$  K higher

---

<sup>1</sup> Arithmetic average composition found in the stellar envelope after the last thermal pulse with third dredge-up of the 1.5, 2, 2.5, and 3  $M_{\odot}$  FRANEK AGB models at  $Z = 0.01, 0.014, \text{ and } 0.02$  (FRUITY database, <http://fruity.oa-teramo.inaf.it:8080/modelli.pl>, Cristallo et al. 2011) and 1.25, 1.8, 3, and 4  $M_{\odot}$  MONASH AGB models at  $Z = 0.01$  and 0.02.

280 than HfC. Both WC and HfC are more refractory than SiC. Thus, one would expect both  
281 elements to fully condense into SiC, or at least in the same proportion. Based on our data, this  
282 appears not to be the case. One way to explain small fractionations between Hf and W is by  
283 having W condense as a metal instead of WC. This can occur if condensation takes place at  
284 pressures higher than  $10^{-4}$  bars and if W in the circumstellar envelope reaches a concentration  
285 of at least 10 times the abundance found in the Solar System (Lodders & Fegley 1995). We  
286 note that the W enrichment factor determined for the KJB fraction is  $\sim 10$ , which is  
287 comparable to the results obtained for other heavy *s*-process elements. However, the single  
288 SiC grains from the LS+LU fraction show an enrichment factor  $< 3$ . Large fractionation  
289 between elements present in SiC relative to the source composition had been previously  
290 observed (e.g., Al/Mg, Sr/Ba, Amari et al. 1995; Ni/Fe, Marhas et al. 2008), but there is still  
291 no satisfactory explanation for these elemental fractionations.

292

293

## 5. THE *s*-PROCESS PATH IN THE W MASS REGION

294 The *s*-process path in the mass region around W is shown in Figure 1. The *s*-process takes  
295 place in the deep He-rich layers of low- and intermediate-mass stars ( $M \sim 0.8\text{--}8 M_{\odot}$ ) during  
296 their asymptotic giant branch (AGB) phase of evolution (e.g., Gallino et al. 1998; Busso et al.  
297 1999; Herwig 2005; Zinner et al. 2006; Cristallo et al. 2009). In low-mass AGB stars of close-  
298 to-solar metallicity, believed to be the site of origin of mainstream SiC grains, the  $^{13}\text{C}(\alpha,$   
299  $n)^{16}\text{O}$  reaction is the main neutron source responsible for the production of the bulk of the *s*-  
300 process AGB yields. It usually operates under radiative conditions at relatively low  
301 temperatures ( $T \sim 0.9 \times 10^8$  K, corresponding to a thermal energy of  $kT \sim 8$  keV), during the  
302 interval between episodic He burning (thermal pulses), and results in low neutron densities

303 ( $10^6 - 10^7$  neutrons  $\text{cm}^{-3}$ ) (Straniero et al. 1995). A second neutron source, the  $^{22}\text{Ne}(\alpha, n)^{25}\text{Mg}$   
304 reaction, is marginally activated during thermal pulses when the maximum temperature at the  
305 bottom of the He-burning shell reaches  $T \sim 3 \times 10^8$  K ( $kT \sim 23$  keV), resulting in high neutron  
306 densities (up to  $\sim 10^{10}$  neutrons  $\text{cm}^{-3}$  in AGB stars of initial mass  $1.5 - 3 M_{\odot}$ ). Although  
307 neutron captures during these short episodes accounts only for a few percent of the total  
308 exposure, they are essential for adjusting the abundance patterns of the  $s$ -process branchings.

309 The production of W in the He-intershell during interpulse and thermal pulse phases is  
310 strongly affected by branchings at  $^{181}\text{Hf}$ ,  $^{182}\text{Hf}$ ,  $^{182}\text{Ta}$ ,  $^{183}\text{Ta}$ , and  $^{185}\text{W}$  (see Fig. 1). The  
311 competition between neutron capture and  $\beta$ -decay at these branching points can be expressed  
312 by a branching factor ( $f_n$ ), calculated from  $f_n = \lambda_n / (\lambda_n + \lambda_{\beta})$ , where  $\lambda_n = N_n v_T \langle \sigma \rangle$ , and  $\lambda_{\beta} =$   
313  $\ln 2 / t_{1/2}$  are the neutron-capture rate and the  $\beta$ -decay rate, respectively. Here,  $N_n$ ,  $v_T$ ,  $\langle \sigma \rangle$ , and  $t_{1/2}$   
314 are the neutron density, the thermal velocity, the Maxwellian-averaged  $(n, \gamma)$  cross section,  
315 and the half-life, respectively. At the typical conditions of operation of the  $^{13}\text{C}(\alpha, n)^{16}\text{O}$   
316 neutron source ( $T \sim 0.9 \times 10^8$  K,  $N_n \sim 10^6 - 10^7$  neutrons  $\text{cm}^{-3}$ ), the  $^{181}\text{Hf}$ ,  $^{182}\text{Ta}$ , and  $^{183}\text{Ta}$   
317 branching factors are very small ( $< 0.2\%$ ,  $1.5\%$ , and  $< 0.1\%$ , respectively, see Fig. 5a),  
318 indicating that  $^{181}\text{Hf}$ ,  $^{182}\text{Ta}$ , and  $^{183}\text{Ta}$  will  $\beta$ -decay to  $^{181}\text{Ta}$ ,  $^{182}\text{W}$ , and  $^{183}\text{W}$ , respectively, rather  
319 than capture a neutron. Hence, the  $s$ -process flow will create  $^{182}\text{W}$ ,  $^{183}\text{W}$ , and  $^{184}\text{W}$  via  $^{181}\text{Hf}(\beta,$   
320  $\nu) ^{181}\text{Ta}(n, \gamma) ^{182}\text{Ta}(\beta, \nu) ^{182}\text{W}(n, \gamma) ^{183}\text{W}(n, \gamma) ^{184}\text{W}$ . The branching point at  $^{185}\text{W}$  also shows a  
321 small probability ( $\sim 1\%$ ) towards  $^{186}\text{W}$  (Fig. 5a), so that no  $^{186}\text{W}$  will be produced during the  
322 activation of the  $^{13}\text{C}$  neutron source.

323 At higher temperatures and neutron density conditions typically found during the AGB  
324 thermal pulses ( $T$  up to  $3 \times 10^8$  K,  $N_n$  up to  $\sim 10^{10}$  neutrons  $\text{cm}^{-3}$ ), the  $s$ -process production of  
325  $^{182}\text{W}$ ,  $^{183}\text{W}$ , and  $^{186}\text{W}$  is different. Under these conditions, the branching factor at  $^{181}\text{Hf}$  is  $\sim$   
326  $10\%$  at  $N_n = 10^{10}$  neutrons  $\text{cm}^{-3}$  (Fig. 5b), marginally feeding  $^{182}\text{Hf}$ . The laboratory half-life of

327  $^{182}\text{Hf}$  is  $8.9 \times 10^6$  yrs (Vockenhuber et al. 2004), but at  $T \sim 8$  keV and 23keV (and electron  
328 density  $\sim 5 \times 10^{26} \text{ cm}^{-3}$ ) it drops to  $\sim 41 \times 10^3$  yrs and 12 yrs, respectively, as a result of  
329 increased thermal populations of low-lying nuclear states (Takahashi & Yokoi 1987). Despite  
330 the enhancement observed in the  $^{182}\text{Hf}$   $\beta$ -decay rate at stellar conditions, its half-life is still  
331 sufficiently long to allow neutron captures to occur. Therefore,  $^{182}\text{Hf}$  captures a neutron rather  
332 than decay during both interpulse and thermal pulse phases. Provided that the  $^{181}\text{Hf}$  branching  
333 point is open, the  $s$ -process flow will proceed via the sequence  $^{181}\text{Hf}(n, \gamma) ^{182}\text{Hf}(n, \gamma) ^{183}\text{Hf}(\beta,$   
334  $\nu) ^{183}\text{Ta}(\beta, \nu) ^{183}\text{W}$ , consequently bypassing  $^{182}\text{W}$ , as well as  $^{183}\text{W}$  if the branching point at  
335  $^{183}\text{Ta}$  is also activated (see below). After the neutron flow ceases,  $^{182}\text{W}$  is marginally produced  
336 by the decay of  $^{182}\text{Hf}$ . Low-mass AGB stars yield  $^{182}\text{Hf}/^{180}\text{Hf}$  ratios of  $\sim 1.79 \times 10^{-2}$ , which  
337 means that the effect of the  $^{181}\text{Hf}$  branching point is marginal. Only a very small shift of  $\sim 1$  to  
338 3% in the  $^{182}\text{W}/^{184}\text{W}$  ratio due to  $^{182}\text{Hf}$  decay is expected if both Hf and W fully condense into  
339 SiC. This shift is likely undetectable given the low  $^{180}\text{Hf}/^{184}\text{W}$  ratios determined here, which  
340 imply a very low  $s$ -process abundance of  $^{182}\text{Hf}$  in the studied SiC grains. Hence, the  
341 observable radiogenic contribution of  $^{182}\text{Hf}$  to its daughter  $^{182}\text{W}$  in the grains would be much  
342 less than 1% and thus too difficult to observe.

343 The  $s$ -process flow that goes through  $^{181}\text{Hf}(\beta, \nu) ^{181}\text{Ta}(n, \gamma) ^{182}\text{Ta}$  encounters two other  
344 branching points at  $^{182}\text{Ta}$  and  $^{183}\text{Ta}$ . The  $^{182}\text{Ta}$  branching point has a temperature dependent  
345 beta-decay rate and a branching factor  $> 80\%$  (Fig. 5b) during the high neutron density  
346 produced by the  $^{22}\text{Ne}$  source, and may cause the  $s$ -process flow to partially bypass  $^{182}\text{W}$ . The  
347 branching factor at  $^{183}\text{Ta}$  is  $\sim 50\%$  at  $T \sim 3 \times 10^8$  K and  $N_n = 10^{10}$  neutrons  $\text{cm}^{-3}$  (Fig. 5b),  
348 causing the  $s$ -process flow to partially bypass  $^{183}\text{W}$ . The branching factor at  $^{185}\text{W}$  is enhanced  
349 similarly to the  $^{182}\text{Ta}$  branching factor during thermal pulses (Fig. 5b), feeding  $^{186}\text{W}$ , which  
350 results in a smaller  $s$ -process contribution to both  $^{186}\text{Os}$  and  $^{187}\text{Os}$ , due to the presence of the

351 long-living nuclei  $^{187}\text{Re}$ . The  $^{186}\text{W}/^{184}\text{W}$  ratios reported here suggest activation of the  
 352 branching point at  $^{185}\text{W}$ . This result is, in principle, in disagreement with  $^{96}\text{Zr}$  depletions  
 353 observed in SiC grains that indicate that the  $^{22}\text{Ne}$  neutron source was weak in the parent stars  
 354 of the grains (Nicolussi et al. 1997; Lugaro et al. 2003). However, at conditions of  $T \sim 23$  keV  
 355 and  $N_n > 5 \times 10^8$  neutrons  $\text{cm}^{-3}$ , the branching point at  $^{95}\text{Zr}$  shows a smaller branching factor  
 356 than  $^{185}\text{W}$  (Fig. 5b). Therefore, at the same conditions, the  $^{185}\text{W}(n, \gamma)^{186}\text{W}$  reaction shows a  
 357 higher probability to occur than the  $^{95}\text{Zr}(n, \gamma)^{96}\text{Zr}$  reaction. Information about the Zr isotopic  
 358 compositions in the same grains measured for W would help to better constrain the physical  
 359 conditions of the *s*-process in the parent stars of the grains.

360 From Figure 1, it can be seen that there is only one path that leads from  $^{179}\text{Hf}$  to  $^{180}\text{Hf}$ <sup>2</sup>, whose  
 361 relative abundances are not affected by any branching point. If a steady flow is achieved  
 362 along the *s*-process path, the local equilibrium approximation applies  $\langle \sigma \rangle_{(A)} N_{s(A)} \sim \langle \sigma \rangle_{(A-1)}$   
 363  $N_{s(A-1)}$ , where  $\langle \sigma \rangle_{(A)}$  is the Maxwellian averaged  $(n, \gamma)$  cross section of the isotope A, and  $N_s$  its  
 364 *s*-process abundance (Clayton 1983). From this simple formulation, we can infer that the ratio  
 365 of the *s*-process contributions to  $^{179}\text{Hf}$  and  $^{180}\text{Hf}$  are approximately equal to the inverse ratios  
 366 of their neutron-capture cross sections. At thermal energies of  $\sim 8$  and 23 keV, the inverse  
 367 ratio of the  $^{179}\text{Hf}/^{180}\text{Hf}$  neutron-capture cross sections yields  $\langle \sigma \rangle_{(^{180}\text{Hf})} / \langle \sigma \rangle_{(^{179}\text{Hf})} = 0.150$  and  
 368 0.175, respectively, with an uncertainty of  $\sim 1.5\%$  (Dillmann et al. 2006). The grain showing  
 369 the most anomalous W and Hf isotopic ratios, LU-41, has  $^{179}\text{Hf}/^{180}\text{Hf} = 0.141 \pm 0.047$ , in very

---

<sup>2</sup> A branching point at  $^{179}\text{Hf}$  may be activated because this stable nucleus becomes unstable in stellar conditions. This effect is insignificant in our context, as the beta-decay half-life of  $^{179}\text{Hf}$  is  $\sim 30$  yrs at  $T = 3 \times 10^8$  K, however, in some conditions it may lead to the production of  $^{180}\text{Ta}$  (actually an isomeric state,  $^{180}\text{Ta}^m$ ), the least abundant nucleus in the Solar System (e.g., Käppeler et al. 2004). A weak *s*-process branching may also be activated via neutron captures on  $^{179}\text{Hf}$ , feeding the  $8^-$  isomeric state in  $^{180}\text{Hf}$  ( $t_{1/2} = 5.5$  h), which then decays to  $^{180}\text{Ta}^m$  (Beer & Ward 1981).

370 good agreement with the ratio expected from the values of neutron-capture cross sections,  
371 thus indicating an almost pure *s*-process signature in this grain.

372

373

## 6. DISCUSSION

374 Figures 6 and 7 show the W and Hf isotopic ratios of the stardust SiC grains together with *s*-  
375 process model predictions for the envelope compositions of low-mass AGB stars. These  
376 predictions represent the mixing between two components, one close to the solar composition,  
377 representing the initial composition of the stellar envelope (in stardust studies this is  
378 traditionally referred to as the N-component), the other with isotopic characteristics close to  
379 those predicted for pure *s*-process (the G-component) (e.g., Zinner et al. 1991; Nicolussi et al.  
380 1997; Savina et al. 2004). The magnitude of the departure from the N-component towards the  
381 G-component depends on the efficiency and the number of mixing episodes, also known as  
382 third dredge-ups (TDUs), which occur when the convective envelope penetrates into the He  
383 intershell zone. The TDU causes newly synthesized  $^{12}\text{C}$  and *s*-processed material to be mixed  
384 into the convective envelope of the star (e.g., Lugaro et al. 2003).

385 Two different sets of models (FRANEC, Cristallo et al. 2009, 2011; MONASH, Karakas  
386 2010, Karakas et al. 2010) with a range of stellar masses ( $1.25 - 4 M_{\odot}$ ) and metallicities ( $Z =$   
387  $0.01, 0.014, \text{ and } 0.02$ ) were investigated. Of relevance here, in the FRANEC code the  
388 neutron-capture cross sections for the W isotopes are taken from Bao et al. (2000), and  
389 correspond to the values published by Macklin et al. (1983) for  $^{182}\text{W}$ ,  $^{183}\text{W}$ ,  $^{184}\text{W}$ , and  $^{186}\text{W}$ ,  
390 and the theoretical value adopted by Bao et al. (2000) for  $^{185}\text{W}$ . In the MONASH code, the  
391 neutron-capture cross sections for the W isotopes are taken from the KADoNiS Database  
392 (Dillmann et al. 2006), and correspond to the values published by Macklin et al. (1983) for

393  $^{182}\text{W}$  and  $^{183}\text{W}$ , Marganiec et al. (2009) for  $^{184}\text{W}$  and  $^{186}\text{W}$ , and Mohr et al. (2004) for  $^{185}\text{W}$ .

394 The models presented here have been selected for  $C/O > 1$  in the envelope so that the  
395 condition for the formation of SiC is satisfied.

396 In spite of all the differences between the two evolutionary codes, which employ a variety of  
397 input physics also concerning mixing and reaction rates (see Cristallo et al. 2009, 2011;  
398 Karakas 2010; and Karakas et al. 2010 for details), the isotopic compositions predicted by the  
399 two sets of models are in fair agreement with one another. Both sets of models present a good  
400 match with the SiC data for the  $^{182}\text{W}/^{184}\text{W}$ ,  $^{183}\text{W}/^{184}\text{W}$ , and  $^{179}\text{Hf}/^{180}\text{Hf}$  ratios (Fig. 6a, c and Fig.  
401 7a, b, d, e). As already demonstrated by Lugaro et al. (2003) in relation to Sr, Zr, and Ba  
402 isotopic ratios, the marginal activation of the  $^{22}\text{Ne}$  neutron source in the thermal pulses is  
403 necessary to best reproduce some of the single SiC data. In the case of  $^{182}\text{W}/^{184}\text{W}$  and  
404  $^{183}\text{W}/^{184}\text{W}$  ratios, the  $^{22}\text{Ne}$  neutron source allows the activation of the  $^{182}\text{Ta}$  and  $^{183}\text{Ta}$  branching  
405 points, lowering the  $^{182}\text{W}/^{184}\text{W}$  and  $^{183}\text{W}/^{184}\text{W}$  ratios. This is clearly illustrated by comparison  
406 in Figure 7d and 7e of the  $1.8 M_{\odot}$  model, where the  $^{22}\text{Ne}$  neutron source is not activated, as  
407 the temperature in the thermal pulses is always below  $2.66 \times 10^8$  K, with the higher mass  
408 models. The SiC grains that are isotopically solar within errors could be explained either as  
409 contamination with solar material, or as originating in a very low-mass star (the  $1.25 M_{\odot}$   
410 model) where TDU episodes can only slightly modify the envelope's pristine composition.  
411 The KJB average measurement is also well explained as the average of different stellar  
412 masses, except that the  $^{183}\text{W}/^{184}\text{W}$  ratio is below the average of the stellar models (Fig. 7b, e).  
413 Also, the  $^{183}\text{W}/^{184}\text{W}$  ratio observed in the most extreme grain, LU-41, is slightly lower than the  
414 lowest predicted value (but note that the error bars are  $1\sigma$ ).

415 On the other hand, most models predict lower  $^{186}\text{W}/^{184}\text{W}$  ratios than those measured in the  
416 grains (Fig. 6b, d and Fig. 7c, f). The model predictions move towards higher  $^{186}\text{W}/^{184}\text{W}$  ratios

417 with increasing number of thermal pulses, particularly for models of higher masses and lower  
418 metallicities, as the  $^{22}\text{Ne}$  neutron source and thus the  $^{185}\text{W}$  branching point are more activated  
419 in these models. However, they fail to reach the observed values. While some ad hoc  
420 solutions may be found for the single grain data (e.g., the  $4 M_{\odot}$  model reaches the  $^{186}\text{W}/^{184}\text{W}$   
421 ratio measured in grain LU-41 and almost also the value observed in grain LU-36, when  
422 considering that the error bars are 1 sigma), the KJB ratio is particularly puzzling; it agrees  
423 with the solar value within a relatively small error while it should represent the average of  
424 different stellar sources with different masses and metallicities, or, in case of contamination,  
425 should sit on the mixing line connecting the models and the solar composition point.

426 A question that needs to be addressed is whether or not a revision of the neutron-capture cross  
427 sections would improve the match between model predictions and the SiC data. For  $^{182}\text{W}$  and  
428  $^{183}\text{W}$ , the uncertainties in the recommended neutron-capture cross sections are very small ( $\sim$   
429 3%), but the measurements are quite old (Macklin et al. 1983) and no revision has been  
430 obtained since. The possibility that the  $^{182}\text{W}$  neutron-capture cross section had been  
431 overestimated by 20%-30% in the past was recently suggested by Wisshak et al. (2006) and  
432 Vockenhuber et al. (2007) based on the observation that the  $^{182}\text{W}$   $r$ -residual shows a  
433 significant positive deviation from the otherwise very smooth  $r$ -process solar abundance  
434 pattern (see Fig. 12 of Wisshak et al. 2006; or Fig. 6 of Vockenhuber et al. 2007). Also, a  
435 smaller  $^{182}\text{Ta}$  neutron-capture cross section, which is based on theoretical calculations with a  
436 relatively large uncertainty ( $\sim 16\%$ ), could lead to a lower  $^{182}\text{Ta}$  branching factor, resulting in  
437 a higher  $s$ -process contribution to  $^{182}\text{W}$  and a lower  $^{182}\text{W}$   $r$ -residual (see Table 13 of  
438 Vockenhuber et al. 2007). However, any major changes resulting in a higher  $^{182}\text{W}$   $s$ -process  
439 production would lead to higher  $^{182}\text{W}/^{184}\text{W}$  ratios and a mismatch with the SiC data reported  
440 here. For example, a 30% reduction of the  $^{182}\text{W}$  cross section in the MONASH  $3 M_{\odot}$  and  $Z =$

441 0.01, and  $3 M_{\odot}$  and  $Z = 0.02$  models results in a  $\sim 35\%$  increase in the final  $^{182}\text{W}/^{184}\text{W}$  ratio in  
442 the stellar envelope, which is well above the values observed in the SiC grains. On the other  
443 hand, our data suggest that a small adjustment (toward lower values) in the *s*-process  
444 production of  $^{183}\text{W}$  is needed in order to obtain a better agreement between our SiC data and  
445 the *s*-process model predictions. This may be achieved by adopting a higher ( $\sim 30\%$ )  $^{183}\text{W}$   
446 neutron-capture cross section.

447 As for the unstable  $^{185}\text{W}$ , its neutron-capture cross section has been recently derived from the  
448 inverse  $^{186}\text{W}(\gamma, n)^{185}\text{W}$  photodisintegration reaction (Sonnabend et al. 2003; Mohr et al. 2004)  
449 with an uncertainty between 10 and 15% and a difference between the two measurements of  
450 24% at 30 keV. These values lead to an overproduction of the solar *s*-only  $^{186}\text{Os}$  of at least  
451 20% (Sonnabend et al. 2003). Several hypotheses have been raised to resolve this puzzle.  
452 Sonnabend et al. (2003) suggested that the stellar model apparently overestimates the  $\beta$ -decay  
453 part and/or underestimates the neutron-capture part of the  $^{185}\text{W}$  branching point. Meyer and  
454 Wang (2007), on the other hand, proposed that this problem could be resolved either by  
455 increasing the  $^{186}\text{Os}$  neutron-capture cross section by  $\sim 20\%$  or by increasing the branching  
456 factor at  $^{186}\text{Re}$ . An increase in the  $^{186}\text{Os}$  neutron-capture cross section would also help in  
457 explaining the low  $^{186}\text{Os}/^{188}\text{Os}$  *s*-process ratio derived from isotopic anomalies observed in  
458 primitive meteorites (Brandon et al. 2005; Yokoyama et al. 2007). However, a recent  
459 measurement of the  $^{186}\text{Os}$  neutron-capture cross section by Mosconi et al. (2010a) excludes  
460 this hypothesis. As noted by Reisberg et al. (2009), the mismatch between the inferred  
461  $^{186}\text{Os}/^{188}\text{Os}$  *s*-process ratio, derived from isotopic anomalies observed in primitive meteorites  
462 (Brandon et al. 2005; Yokoyama et al. 2007), and model predictions could be resolved by  
463 using a recent measurement of the  $^{188}\text{Os}$  neutron-capture cross section (Mosconi et al. 2007),  
464 which is  $\sim 27\%$  lower than the recommended value of Bao et al. (2000). Sonnabend et al.

465 (2003) suggested an increase of the  $^{185}\text{W}$  neutron-capture cross section (by about 60%), which  
466 would lead to a decrease of  $^{186}\text{Os}$  and an increase of the  $^{186}\text{W}$  abundance. We computed AGB  
467 models using the recommended  $^{185}\text{W}$  neutron-capture cross section multiplied by a factor of 2  
468 to see if this very large change would help in matching the  $^{186}\text{W}/^{184}\text{W}$  grain data. We obtain an  
469 increase of  $\sim 20\%$  in the final  $^{186}\text{W}/^{184}\text{W}$  ratio in the stellar envelope of the MONASH  $3 M_{\odot}$   
470 and  $Z = 0.01$ , and  $3 M_{\odot}$  and  $Z = 0.02$  models, but it still lower than the observed stardust SiC  
471 data.

472 We also checked the impact of the uncertainties in the  $\beta$ -decay rates of the unstable isotopes  
473  $^{181}\text{Hf}$ ,  $^{182}\text{Ta}$ , and  $^{185}\text{W}$ . At a temperature of  $3 \times 10^8$  K, Goriely (1999) reported uncertainties of  
474 roughly a factor of three for  $^{181}\text{Hf}$  and  $^{182}\text{Ta}$  and of roughly 40% for  $^{185}\text{W}$ . Variations were  
475 found to be small, at most 20% in the  $^{182}\text{W}/^{184}\text{W}$  ratios, mostly due to the uncertainties in the  
476 decay rate of  $^{182}\text{Ta}$ . Further, we checked the impact of the uncertainties in the theoretical  
477 neutron-capture cross sections of  $^{181}\text{Hf}$  and  $^{182}\text{Ta}$  by considering the theoretical estimates  
478 reported in the KADoNiS Database (Dillmann et al. 2006) on the basis of different codes used  
479 to compute the rates. These uncertainties do not lead to significant variations on the model  
480 predictions, at most 16% in the  $^{182}\text{W}/^{184}\text{W}$  ratios when the neutron-capture cross section of  
481  $^{182}\text{Ta}$  was varied by a factor of two.

482 In summary, the SiC data do not support the problem of the  $s$ -process underproduction of  
483  $^{182}\text{W}$  that follows from the high solar  $r$ -process residual. However, it is important to note that  
484 the  $r$ -process residuals are calculated from  $s$ -process predictions obtained from one stellar  
485 model (or at most from the average of two different masses at the same metallicity, e.g.,  
486 Arlandini et al. 1999) or from phenomenological models (e.g. Käppeler et al. 1982). A more  
487 realistic approach would be to derive them from models of the chemical evolution of the  
488 Galaxy (e.g., Travaglio et al. 1999). This is because the Solar System composition is the

489 result of nucleosynthesis from many generations of AGB stars of many different masses and  
490 metallicities. This more realistic description of the solar *s*-process abundances and of the *r*-  
491 process residuals may help solving the discrepancies found in the Hf-Ta-W-Re-Os mass  
492 region and needs to be pursued.

493 The SiC data qualitatively support the solution of the  $^{186}\text{Os}$  overproduction problem according  
494 to which the  $^{185}\text{W}$  branching point should be activated more strongly. However, while the  
495  $^{186}\text{Os}$  problem is solved by increasing the neutron-capture cross section of  $^{185}\text{W}$  by  $\sim 60\%$   
496 (Sonnabend et al. 2003), our models do not match the SiC data even if this cross section is  
497 increased by a factor of two! Another way to increase the  $^{186}\text{W}/^{184}\text{W}$  ratio would be to  
498 decrease the production of  $^{184}\text{W}$ . The  $^{186}\text{W}$  nuclide is created during thermal pulses, when the  
499  $^{185}\text{W}$  branching point is open. In contrast,  $^{184}\text{W}$  is created within the  $^{13}\text{C}$  pocket during the  
500 radiative  $^{13}\text{C}$  burning. Thus, the production of  $^{184}\text{W}$  is directly correlated with the  $^{13}\text{C}$  (and  $^{14}\text{N}$ )  
501 abundances within the pocket, which in turn depend on the mixing mechanism that allows a  
502 few protons to penetrate from the envelope during the TDU into the underlying  $^{12}\text{C}$  rich  
503 intershell. The current uncertainties affecting this mixing are still large, so that a clear  
504 description is still not available and the amount of  $^{13}\text{C}$  in the pocket may still be treated as a  
505 free parameter. In the FRANEC code, the  $^{13}\text{C}$  abundance within the pocket is derived from the  
506 application of an exponentially decreasing profile of convective velocities at the inner border  
507 of the convective envelope. In the MONASH code, the  $^{13}\text{C}$  abundance within the pocket is  
508 derived from artificial inclusion of an exponentially decreasing abundance of protons in the  
509 He intershell. The inclusion of physical mechanisms not explicitly treated in our codes, such  
510 as rotation, could modify the  $^{13}\text{C}$  and  $^{14}\text{N}$  abundances within the pocket before and during the  
511 activation of the  $^{13}\text{C}(\alpha, n)^{16}\text{O}$  reaction, thus leading to different  $^{186}\text{W}/^{184}\text{W}$  ratios. For example,  
512 the calculations of Arlandini et al. (1999) used a very different  $^{13}\text{C}$  pocket than ours and

513 produced  $^{186}\text{W}/^{184}\text{W} = 0.66$  (together with  $^{183}\text{W}/^{184}\text{W} = 0.35$ ). However, these models were  
514 targeted specifically to match the  $s$ -only solar distribution and are hence not appropriate to be  
515 compared to the composition of stardust SiC grains. In order to test the effects of a different  
516  $^{13}\text{C}$  profile in our calculations, we changed in the MONASH 3  $M_{\odot}$ ,  $Z = 0.02$  model the extent  
517 in mass of the  $^{13}\text{C}$  pocket from  $0.002 M_{\odot}$  to  $0.0005 M_{\odot}$ . We obtained  $^{186}\text{W}/^{184}\text{W} = 0.58$ ,  
518 however the  $^{183}\text{W}/^{184}\text{W}$  ratio is also closer to the solar value (0.43).

519 Note that although our SiC data allowed us to address some discrepancies found in the solar  
520  $s$ - and  $r$ -abundance distributions in the Hf-Ta-W-Re-Os mass region, the stardust grains  
521 provide a more direct constraint on the  $s$ -process in low-mass AGB stars rather than the solar  
522  $s$ -process component. Furthermore, the calculation of solar  $s$ - and  $r$ -abundance distributions  
523 suffers from significant uncertainties. Goriely (1999) used an extended parametric  $s$ -process  
524 model, the "multi-event  $s$ -process" model described in Goriely (1997), to analyse the impact  
525 of nuclear and observational uncertainties on the solar  $r$ -process residual distribution. The  
526 final result, presented in Figure 8 of Goriely (1999), clearly shows that the smoothness of the  
527  $r$ -process residual curve in the Hf-Ta-W-Re-Os region is well reproduced within the  
528 uncertainties. This would still be true when considering the new measurements of the Hf  
529 neutron-capture cross-sections of Wisshak et al. (2006), which result in a downward shift of  
530 the  $r$ -residual of  $^{180}\text{Hf}$ . There are other uncertainty factors that may also affect the solar  $s$ - and  
531  $r$ -abundances predictions, like those arising from galactic and stellar evolution models. The  
532 combined effect of all uncertainties precludes any definite conclusion about the solar  $s$ - and  $r$ -  
533 abundance distributions to be made to the level needed for a detailed comparison with the  
534 stardust data.

535

## 7. CONCLUSIONS

536

537 We report the first W isotopic anomalies in mainstream stardust SiC grains recovered from  
538 the Murchison carbonaceous chondrite. Comparisons between grain data and *s*-process model  
539 predictions for the envelope compositions of low-mass AGB stars show that a single choice  
540 of stellar mass and metallicity cannot account for the range of isotopic ratios observed in the  
541 SiC grains. There is an overall match between the SiC data and the theoretical predictions for  
542 the  $^{182}\text{W}/^{184}\text{W}$  and  $^{183}\text{W}/^{184}\text{W}$  ratios, particularly if a 30% higher neutron-capture cross section  
543 is employed for  $^{183}\text{W}$ . However, the AGB models fail to reproduce the high  $^{186}\text{W}/^{184}\text{W}$  ratios  
544 observed in the grains. We note, however, that many uncertainties affect stellar evolutionary  
545 computations of the *s*-process. Among them are the formation of the  $^{13}\text{C}$  pocket, the mass-loss  
546 law, the TDU, and the efficiency of the  $^{22}\text{Ne}$  neutron source. For example, the inclusion of  
547 rotation and magnetic fields may affect the operation of the  $^{13}\text{C}$  neutron source, and a lower  
548 efficiency of this neutron source may decrease the production of  $^{184}\text{W}$ , thus increasing the  
549  $^{183}\text{W}/^{184}\text{W}$  ratio. Also a milder mass-loss history would lead to a larger number of thermal  
550 pulses and, therefore, possibly to a larger  $^{186}\text{W}/^{184}\text{W}$  ratio. Similarly, an increase of the  $^{22}\text{Ne}(\alpha,$   
551  $n)$  cross section could lead to a higher neutron density, thus increasing the  $^{186}\text{W}$  production,  
552 but perhaps worsening the match with the  $^{96}\text{Zr}/^{94}\text{Zr}$  ratio observed in the grains (Lugaro et al.  
553 2003). We intend to explore these hypotheses in the future. Finally, further W isotopic  
554 measurements with better precision on additional grains would be extremely helpful. They  
555 could shed light on the possibility of contamination affecting the current W measurements  
556 and confirm the high  $^{186}\text{W}/^{184}\text{W}$  ratios reported here.

557

558

ACKNOWLEDGEMENTS

559

560 J.N. Ávila was supported by a Ph.D. scholarship (Grant#200081/2005-5) of the Brazilian  
561 National Council for Scientific and Technological Development (CNPq). She acknowledges  
562 the Australian National University through an ANU Vice-Chancellor's Higher Degree  
563 Research Travel Grant. M. Lugaro is an ARC Future Fellow and a Monash Research Fellow.  
564 T. R. Ireland acknowledges support by ARC grants DP0342772 and DP0666751. E. Zinner  
565 acknowledges support by NASA grant NNX08AG71G. S. Cristallo acknowledges support by  
566 the Spanish Grant AYA2008-04211-C02-02 and FPA2008-03908 from the MEC. S. Cristallo  
567 thanks Roberto Gallino for fruitful scientific discussions. We are grateful to Roy Lewis for  
568 providing the LS+LU grains. We thank an anonymous referee for their comments and Eric  
569 Feigelson for handling of this manuscript.

570

REFERENCES

- 571
- 572
- 573 Amari, S., Hoppe, P., Zinner, E. K., & Lewis, R. S. 1995, *Meteorit. Planet. Sci.*, 30, 679
- 574 Amari, S., Lewis, R. S., & Anders, E. 1994, *Geochimic. Cosmochim. Acta*, 58, 459
- 575 Amari, S., Zinner, E. K., & Lewis, R. S. 2000, *Meteorit. Planet. Sci.*, 35, 997
- 576 Anders, E., & Grevesse, N. 1989, *Geochimic. Cosmochim. Acta*, 53, 197
- 577 Arlandini, C., Käppeler, F., Wisshak, K., Gallino, R., Lugaro, M., Busso, M., & Straniero, O.
- 578 1999, *ApJ*, 525, 88
- 579 Bao, Z. Y., Beer, H., Käppeler, F., Voss, F., Wisshak, K., & Rauscher, T. 2000, *At. Data*
- 580 *Nucl. Data Tables*, 76, 70
- 581 Beer, H. & Ward, R. A. 1981, *Nature*, 291, 308
- 582 Brandon, A. D., Humayun, M., Puchtel, I. S., Leya, I., & Zolensky, M. 2005, *Science*, 309,
- 583 1233
- 584 Busso, M., Gallino, R., & Wasserburg, G. J. 1999, *ARA&A*, 37, 239
- 585 Clayton, D. D. 1983, *Principles of stellar evolution and nucleosynthesis* (Chicago: The
- 586 University of Chicago Press)
- 587 Clayton, D. D. & Nittler, L. R. 2004, *ARA&A*, 42, 39
- 588 Cristallo, S., Piersanti, L., Straniero, O., Gallino, R., Domínguez, I., Abia, C., Di Rico, G.,
- 589 Quintini, M., & Bisterzo, S. 2011, *ApJS*, accepted (arXiv1109.1176C)
- 590 Cristallo, S., Straniero, O., Gallino, R., Piersanti, L., Domínguez, I., & Lederer, M. T. 2009,
- 591 *ApJ*, 696, 797

- 592 Cyburt, R. H. et al. 2010, *ApJS*, 189, 240
- 593 Dillmann, I., Heil, M., Käppeler, F., Plag, R., Rauscher, T., & Thielemann, F.-K. 2006, in  
594 Capture Gamma-Ray Spectroscopy and Related Topics, ed. A. Woehr & A. Aprahamian  
595 (New York: AIP) 819, 123
- 596 Dodson, M. H. 1978, *J. Phys. E Sci. Instrum.*, 11, 296
- 597 Fujii, K. et al. 2010, *Phys. Rev. C*, 82, 015804
- 598 Gallino, R., Arlandini, C., Busso, M., Lugaro, M., Travaglio, C., Straniero, O., Chieffi, A., &  
599 Limongi, M. 1998, *ApJ*, 497, 388
- 600 Goriely, S. 1997, *A&A*, 327, 845
- 601 Goriely, S. 1999, *A&A*, 342, 881
- 602 Gyngard, F., Amari, S., Zinner, E. K., & Ott, U. 2009a, *Publ. Astron. Soc. Australia*, 26, 278
- 603 Gyngard, F., Amari, S., Zinner, E. K., & Ott, U. 2009b, *ApJ*, 694, 359
- 604 Hayakawa, T., Shizuma, T., Kajino, T., Chiba, S., Shinohara, N., Nakagawa, T., & Arima, T.  
605 2005, *ApJ*, 628, 533
- 606 Heck, P. R., Gyngard, F., Ott, U., Matthias, M., Ávila, J. N., Amari, S., Zinner, E. K., Lewis,  
607 R. S., Baur, H., & Wieler, R. 2009, *ApJ*, 698, 1155
- 608 Herwig, F. 2005, *ARA&A*, 43, 435
- 609 Hoppe, P., Amari, S., Zinner, E. K., Ireland, T., & Lewis, R. S. 1994, *ApJ*, 430, 870
- 610 Huss, G. R., Ogliore, R. C., Nagashima, K., Telus, M., & Jilly, C. E. 2011, *Lunar Planet. Sci.*  
611 *Conf*, 42, 2608
- 612 Hynes, K. M., & Gyngard, F. 2009, *Lunar Planet. Sci. Conf*, 40, 1198
- 613 Ireland, T. R., Zinner, E. K., & Amari, S. 1991, *ApJ*, 376, L53

- 614 Jacobsen, S. 2005, *Annu. Rev. Earth Planet. Sci.*, 33, 531
- 615 Käppeler, F., Arlandini, C., Heil, M., Voss, F., Wisshak, K., Reifarth, R., Straniero, O.,  
616 Gallino, R., Masera, S., & Travaglio, C. 2004, *Phys. Rev. C*, 69, 055802
- 617 Käppeler, F., Beer, H., Wisshak, K., Clayton, D. D., Macklin, R. L., & Ward, R. A. 1982,  
618 *ApJ*, 257, 821
- 619 Karakas, A. I. 2010, *MNRAS*, 403, 1413
- 620 Karakas, A. I., Campbell, S. W., & Stancliffe, R. J. 2010, *ApJ*, 713, 374
- 621 Kashiv, Y. 2004, PhD thesis, The University of Chicago
- 622 Kinny, P. D., Compston, W., & Williams, I. S. 1991, *Geochimic. Cosmochim. Acta*, 55, 849
- 623 Lodders, K. 2003, *ApJ*, 591, 1220
- 624 Lodders, K. 2010, in *Principles and Perspectives in Cosmochemistry*, ed. A. Goswami & B.  
625 E. Reddy (Berlin: Springer), 379
- 626 Lodders, K. & Amari, S. 2005, *Chem. Erde*, 65, 93
- 627 Lodders, K., & Fegley, B. 1995, *Meteorit. Planet. Sci.*, 30, 661
- 628 Lugaro, M., Davis, A. M., Gallino, R., Pellin, M. J., Straniero, O., & Käppeler, F. 2003, *ApJ*,  
629 593, 486
- 630 Macklin, R., Drake, M., & Arthur, E. 1983, *NSE*, 98
- 631 Marganiec, J., Dillmann, I., Domingo Pardo, C., & Käppeler, F. 2009, *Phys. Rev. C*, 80,  
632 025804
- 633 Marhas, K. K., Amari, S., Gyngard, F., Zinner, E. K., & Gallino, R. 2008, *ApJ*, 689, 622
- 634 Meyer, B. S., & Wang, C. 2007, *Lunar Planet. Sci. Conf.*, 38, 2055

- 635 Mohr, P., Shizuma, T., Ueda, H., Goko, S., Makinaga, A., Hara, K. H., Hayakawa, T., Lui,  
636 Y.-W., Ohgaki, H., & Utsunomiya, H. 2004, *Phys. Rev. C*, 69, 032801
- 637 Mosconi, M., et al. 2010a, *Phys. Rev. C*, 82, 015802
- 638 Mosconi, M., Heil, M., Käppeler, F., Plag, R., & Mengoni, A. 2010b, *Phys. Rev. C*, 82,  
639 015803
- 640 Mosconi, M., et al. 2007, *Prog. Part. Nucl. Phys.*, 59, 165
- 641 ---. 2006, in *Nuclei in the Cosmos IX: Ninth Int. Symp. on Nuclear Astrophysics*, PoS(NIC-  
642 IX)055
- 643 Nicolussi, G. K., Davis, A. M., Pellin, M. J., Lewis, R. S., Clayton, R. N., & Amari, S. 1997,  
644 *Science*, 277, 1281
- 645 Nicolussi, G. K., Pellin, M. J., Lewis, R. S., Davis, A. M., Amari, S., & Clayton, R. N. 1998a,  
646 *Geochimic. Cosmochim. Acta*, 62, 1093
- 647 Nicolussi, G. K., Pellin, M. J., Lewis, R. S., Davis, A. M., Clayton, R. N., & Amari, S. 1998b,  
648 *Phys. Rev. Lett.* 81, 3583
- 649 Ogliore, R. C., Huss, G. R., & Nagashima, K. 2011, *Nucl. Instrum. Methods Phys. Res. B*,  
650 269, 1910
- 651 Qin, L., Dauphas, N., Wadhwa, M., Markowski, A., Gallino, R., Janney, P. E., & Bouman, C.  
652 2008, *ApJ*, 674, 1234
- 653 Reisberg, L., Dauphas, N., Luguet, A., Pearson, D., Gallino, R., & Zimmermann, C. 2009,  
654 *Earth Planet. Scie. Lett.*, 277, 334
- 655 Savina, M. R., Davis, A. M., Tripa, C. E., Pellin, M. J., Clayton, R. N., Lewis, R. S., Amari,  
656 S., Gallino, R., & Lugaro, M. 2003, *Geochimic. Cosmochim. Acta*, 67, 3201

- 657 Savina, M. R., Davis, A. M., Tripa, C. E., Pellin, M. J., Gallino, R., Lewis, R. S., & Amari, S.  
658 2004, *Science*, 303, 649
- 659 Segawa, M., Masaki, T., Nagai, Y., Temma, Y., Shima, T., Mishima, K., Igashira, M.,  
660 Goriely, S., Koning, A., & Hilaire, S. 2007, *Phys. Rev. C*, 76, 022802
- 661 Sonnabend, K., Mohr, P., Vogt, K., Zilges, A., Mengoni, A., Rauscher, T., Beer, H.,  
662 Käppeler, F., & Gallino, R. 2003, *ApJ*, 583, 506
- 663 Straniero, O., Gallino, R., Busso, M., Chieffi, A., Raiteri, C. M., Limongi, M., & Salaris, M.  
664 1995, *ApJ*, 440, L85
- 665 Takahashi, K., & Yokoi, K. 1987, *At. Data Nucl. Data Tables*, 36, 375
- 666 Travaglio, C., Galli, D., Gallino, R., Busso, M., Ferrini, F., & Straniero, O. 1999, *ApJ*, 521,  
667 691
- 668 Virag, A., Wopenka, B., Amari, S., Zinner, E. K., Anders, E., & Lewis, R. S. 1992,  
669 *Geochimic. Cosmochim. Acta*, 56, 1715
- 670 Vockenhuber, C., Dillmann, I., Heil, M., Käppeler, F., Winckler, N., Kutschera, W., Wallner,  
671 A., Bichler, M., Dababneh, S., Bisterzo, S., & Gallino, R. 2007, *Phys. Rev. C*, 75, 015804
- 672 Vockenhuber, C., Oberli, F., Bichler, M., Ahmad, I., Quitté, G., Meier, M., Halliday, A., Lee,  
673 D.-C., Kutschera, W., Steier, P., Gehrke, R., & Helmer, R. 2004, *Phys. Rev. Lett.*, 93,  
674 172501
- 675 Wisshak, K., Voss, F., Käppeler, F., Kazakov, L., Bečvář, F., Krτίčka, M., Gallino, R., &  
676 Pignatari, M. 2006, *Phys. Rev. C*, 73, 045807
- 677 Yokoyama, T., Alexander, C. M. O., & Walker, R. J. 2011, *Earth Planet. Scie. Lett.*, 305, 115

- 678 Yokoyama, T., Rai, V., Alexander, C., Lewis, R., Carlson, R., Shirey, S., Thiemens, M., &  
679 Walker, R. 2007, *Earth Planet. Scie. Lett.*, 259, 567
- 680 Zinner, E. K. 1998, *Ann. Rev. Earth Plant. Sci.* 26, 147
- 681 ---. 2004 (online update 2007), in *Treatise on Geochemistry*, Vol. 1, Meteorites, Planets, and  
682 Comets, ed. A. M. Davis, H. D. Holland, & K. K. Turekian (Oxford: Pergamon), 17
- 683 Zinner, E. K., Amari, S., & Lewis, R. S. 1991, *ApJ*, 382, L47
- 684 Zinner, E. K., Nittler, L. R., Gallino, R., Karakas, A., Lugaro, M., Straniero, O., & Lattanzio,  
685 J. 2006, *ApJ*, 650, 350
- 686

687 FIGURE CAPTIONS

688 Figure 1: Part of the nuclide chart showing the *s*-process nucleosynthesis path in the region of  
689 Hf-Ta-W-Re-Os (modified from Hayakawa et al. 2005; and Dillmann et al. 2006).  
690 Percent abundances (non-italic) are shown for each stable isotope (solid boxes) and  
691 laboratory half-lives (italic) for each unstable isotope (dashed line boxes). Half-lives  
692 at stellar temperatures may be different, as discussed in the text. The main *s*-process  
693 path is shown as a bold line and branches and secondary paths are shown as finer  
694 lines, *s*-only isotope  $^{186}\text{Os}$  is indicated by a bold box.

695 Figure 2: Silicon-, C-, and N-isotopic ratios of stardust SiC grains from the LS+LU fraction  
696 (white squares, from Virag et al. 1992) analysed in the present study. Data for  
697 mainstream SiC grains from previous analyses (Hynes & Gyngard 2009) are shown  
698 for comparison (grey squares). Data for the SiC-enriched bulk sample (KJB fraction,  
699 black square) from Amari et al. (2000) are also plotted. Error bars from previous  
700 measurements are omitted for clarity. Black dashed lines indicate the solar ratios  
701 (Lodders 2010) as inferred from terrestrial composition. (a) Si-isotopic ratios  
702 expressed as deviations ( $\delta$ -values) from the reference terrestrial (=solar) isotopic  
703 composition in parts per thousand (‰). Error bars are smaller than the symbols.  
704 Also shown is the so-called mainstream correlation line indicated by the solid line,  
705 with slope of 1.35 (Zinner et al. 2006). (b)  $^{14}\text{N}/^{15}\text{N}$  ratios plotted against  $^{12}\text{C}/^{13}\text{C}$   
706 ratios. Error bars are smaller than the symbols.

707 Figure 3: SHRIMP-RG mass scans of  $^{182}\text{W}^{16}\text{O}^+$  (a),  $^{183}\text{W}^{16}\text{O}^+$  (b),  $^{184}\text{W}^{16}\text{O}^+$  (c), and  $^{186}\text{W}^{16}\text{O}^+$   
708 (d), obtained in NIST-610 silicate glass, a “pure” synthetic SiC, and a SiC ceramic  
709 doped with heavy elements. Energy offset = 0 eV and  $m/\Delta m \sim 7000$  (at 10% peak).

710 Figure 4: Tungsten isotopic compositions determined for the SiC-enriched sample (KJB  
711 fraction). Each bar represents an individual measurement. Bold and dashed lines  
712 indicate solar ratios (as inferred from terrestrial composition, Jacobsen 2005) and  
713 SiC weighted mean ratios, respectively. Box heights are  $2\sigma$ . Weighted means are  
714 also reported as deviations ( $\delta$ -values) from the reference terrestrial (=solar) isotopic  
715 composition in parts per thousand (‰). MSWD = mean square weighted deviation.

716 Figure 5: Branching factor ( $f_n$ ) of  $^{181}\text{Hf}$ ,  $^{182}\text{Hf}$ ,  $^{182}\text{Ta}$ ,  $^{183}\text{Ta}$ ,  $^{185}\text{W}$ , and  $^{95}\text{Zr}$  at  $kT = 8$  keV (a)  
717 and 23 keV (b) as a function of neutron density. We used the  $\beta$ -decay rates reported  
718 by Takahashi & Yokoi (1987) and the latest accepted neutron-capture rates from the  
719 KADoNiS Database (<http://www.kadonis.org/>; Dillmann et al. 2006), except for the  
720  $^{183}\text{Ta}$ , where the neutron-capture rate from JINA REACLIB database  
721 (<http://groups.nsl.msui.edu/jina/reactlib/db/>; Cyburt et al. 2010) was used. All values  
722 were calculated for an electron density of  $5 \times 10^{26} \text{ cm}^{-3}$ . The branching factor (%)  
723 depends on the neutron-capture and  $\beta^-$  decay rates and indicates the probability that  
724 an unstable isotope will capture a neutron rather than decay. The grey area in (a) and  
725 (b) corresponds to the conditions typically found during interpulse and thermal pulse  
726 phases, respectively, in low-mass AGB stars.

727 Figure 6: (a, c)  $^{182}\text{W}/^{184}\text{W}$  plotted against  $^{183}\text{W}/^{184}\text{W}$  and (b, d)  $^{186}\text{W}/^{184}\text{W}$  plotted against  
728  $^{183}\text{W}/^{184}\text{W}$  for the SiC-enriched sample (KJB fraction) and single SiC grains (LS+LU  
729 fraction). Error bars are  $1\sigma$ . The grey dashed lines in each plot give the best linear fit  
730 through all single SiC grains and the SiC-enriched sample. The black solid lines  
731 shown in each plot give the best linear fit through grains LU-36 and LU-41, and the  
732 SiC-enriched sample; grains LU-34, LU-32, and LU-20 were not included in the fit  
733 because their W isotopic signature may be affected by contamination with solar

734 material. Black dashed lines indicate the solar ratios (as inferred from terrestrial  
735 composition, Jacobsen 2005). SiC data are compared with *s*-process model  
736 predictions (FRANEC and MONASH models) for the envelope compositions of  
737 low-mass AGB stars of different masses and metallicities (see text for details).  
738 Predictions are only plotted when the C/O in the stellar envelope reaches values  
739 higher than 1.

740 **Figure 7:** (a, d)  $^{182}\text{W}/^{184}\text{W}$  versus  $^{179}\text{Hf}/^{180}\text{Hf}$ , (b, e)  $^{183}\text{W}/^{184}\text{W}$  versus  $^{179}\text{Hf}/^{180}\text{Hf}$ , and (c, f)  
741  $^{186}\text{W}/^{184}\text{W}$  versus  $^{179}\text{Hf}/^{180}\text{Hf}$  for the SiC-enriched sample (KJB fraction) and single  
742 SiC grains (LS+LU fraction). Error bars are  $1\sigma$ . The gray dashed lines in each plot  
743 give the best linear fit through all single SiC grains and the SiC-enriched sample.  
744 The black solid lines shown in each plot give the best linear fit through grain LU-41  
745 and the SiC-enriched sample; grains LU-34 and LU-32 were not included in the fit  
746 because their W isotopic signature may be affected by contamination with solar  
747 material. Black dashed lines indicate the solar ratios (as inferred from terrestrial  
748 composition, Jacobsen 2005 and Lodders 2010). SiC data are compared with *s*-  
749 process model predictions (FRANEC and MONASH models) for the envelope  
750 compositions of low-mass AGB stars of different masses and metallicities (see text  
751 for details). Predictions are only shown when the C/O in the stellar envelope reaches  
752 values higher than 1.

753

754 **Table 1:** C-, N- and Si-isotopic compositions of stardust SiC grains from the KJB and  
 755 LS+LU fractions measured for W and Hf isotopes. Isotopic ratios are reproduced from Amari  
 756 et al. (2000) and Virag et al. (1992). Errors are  $1\sigma$ .

757

Grain/ Spot	Size ( $\mu\text{m}$ )	$^{12}\text{C}/^{13}\text{C}$ $\pm 1\sigma$	$^{14}\text{N}/^{15}\text{N}$ $\pm 1\sigma$	$\delta^{29}\text{Si}/^{28}\text{Si}$ <sup>a</sup> $\pm$ $1\sigma$ (‰)	$\delta^{30}\text{Si}/^{28}\text{Si}$ <sup>a</sup> $\pm$ $1\sigma$ (‰)
KJB fraction (Murchison SiC-enriched sample)					
KJB	0.49	$37.0 \pm 0.4$	$521 \pm 60$	$24.6 \pm 1.3$	$37.8 \pm 3.4$
LS+LU fraction (Murchison single grains)					
LU-34	7 x 9	$54.3 \pm 0.4$	$1889 \pm 13$	$86.4 \pm 3.0$	$73.2 \pm 3.4$
LU-36	23 x 23	$49.1 \pm 0.4$	$408 \pm 20$	$37.9 \pm 2.5$	$41.1 \pm 3.1$
LU-32	5 x 13	$63.0 \pm 0.4$	$1088 \pm 14$	$55.3 \pm 2.5$	$47.8 \pm 3.2$
LU-20	15 x 26	$48.6 \pm 0.4$	$935 \pm 22$	$38.6 \pm 2.6$	$45.0 \pm 3.5$
LU-41	13 x 13	$48.4 \pm 0.3$	$678 \pm 15$	$43.3 \pm 3.4$	$44.3 \pm 2.9$

758

$$^a \delta^i\text{Si}/^{28}\text{Si} (\text{‰}) = [({}^i\text{Si}/^{28}\text{Si})_{\text{measured}}/({}^i\text{Si}/^{28}\text{Si})_{\text{solar}} - 1] \times 10^3.$$

759

**Table 2:** Tungsten and hafnium isotopic ratios determined in stardust SiC grains. Errors are  $1\sigma$ .

Spot/ Grain	$^{182}\text{W}/^{184}\text{W}$ $\pm 1\sigma$	$\delta^{182}\text{W}/^{184}\text{W}^b$ $\pm 1\sigma$ (‰)	$^{183}\text{W}/^{184}\text{W}$ $\pm 1\sigma$	$\delta^{183}\text{W}/^{184}\text{W}^b$ $\pm 1\sigma$ (‰)	$^{186}\text{W}/^{184}\text{W}$ $\pm 1\sigma$	$\delta^{186}\text{W}/^{184}\text{W}^b$ $\pm 1\sigma$ (‰)	$^{179}\text{Hf}/^{180}\text{Hf}$ $\pm 1\sigma$	$\delta^{179}\text{Hf}/^{180}\text{Hf}^c$ $\pm 1\sigma$ (‰)	$^{180}\text{Hf}/^{184}\text{W}^d$ $\pm 1\sigma$
Terrestrial <sup>a</sup>	0.865		0.467		0.928		0.388		1.302
KJB fraction (Murchison SiC-enriched sample)									
KJB-01	0.725 ± 0.054	-162 ± 63	0.395 ± 0.027	-154 ± 57	0.755 ± 0.077	-186 ± 83	n.a.		n.a.
KJB-02	0.824 ± 0.044	-48 ± 51	0.434 ± 0.050	-70 ± 108	0.858 ± 0.052	-76 ± 56	n.a.		0.095 ± 0.013
KJB-03	0.817 ± 0.024	-56 ± 28	0.399 ± 0.015	-147 ± 31	0.985 ± 0.029	62 ± 31	n.a.		0.046 ± 0.002
KJB-04	0.752 ± 0.045	-130 ± 52	0.395 ± 0.029	-154 ± 62	0.904 ± 0.056	-25 ± 60	n.a.		0.041 ± 0.004
KJB-05	0.825 ± 0.043	-46 ± 50	0.394 ± 0.026	-157 ± 57	0.954 ± 0.054	28 ± 58	n.a.		0.097 ± 0.015
KJB-06	0.838 ± 0.056	-31 ± 64	0.461 ± 0.037	-12 ± 78	0.963 ± 0.044	39 ± 47	n.a.		0.059 ± 0.009
KJB-07	0.845 ± 0.055	-23 ± 63	0.454 ± 0.036	-28 ± 76	0.995 ± 0.065	72 ± 70	n.a.		0.057 ± 0.012
KJB-08	0.829 ± 0.058	-42 ± 67	0.451 ± 0.038	-35 ± 80	0.996 ± 0.068	74 ± 72	n.a.		0.068 ± 0.007
KJB-09	0.817 ± 0.056	-55 ± 64	0.436 ± 0.036	-66 ± 77	0.902 ± 0.064	-28 ± 69	0.338 ± 0.060	-130 ± 155	0.069 ± 0.007
KJB-10	n.a.		n.a.		n.a.		0.318 ± 0.059	-181 ± 153	n.a.
KJB-11	n.a.		n.a.		n.a.		0.322 ± 0.056	-170 ± 144	n.a.
<i>Weighted average</i>	0.809 ± 0.014	-64 ± 17	0.411 ± 0.009	-120 ± 22	0.944 ± 0.024	18 ± 26	0.326 ± 0.033	-160 ± 85	0.050 ± 0.005
LS+LU fraction (Murchison single grains)									
LU-34	0.866 ± 0.067	1 ± 77	0.485 ± 0.044	38 ± 95	0.887 ± 0.069	-44 ± 75	0.475 ± 0.076	223 ± 195	0.194 ± 0.035
LU-36	0.722 ± 0.070	-165 ± 80	0.384 ± 0.061	-177 ± 130	0.802 ± 0.091	-136 ± 98	b.d.l.		0.070 ± 0.009
LU-32	0.848 ± 0.072	-20 ± 83	0.463 ± 0.048	-8 ± 102	0.870 ± 0.076	-62 ± 81	0.437 ± 0.078	126 ± 200	0.203 ± 0.016
LU-20	0.802 ± 0.071	-73 ± 83	0.439 ± 0.042	-61 ± 89	0.769 ± 0.070	-171 ± 76	b.d.l.		0.111 ± 0.030
LU-41	0.648 ± 0.056	-250 ± 65	0.304 ± 0.034	-349 ± 73	0.639 ± 0.058	-312 ± 63	0.141 ± 0.047	-637 ± 121	0.276 ± 0.047

<sup>a</sup>  $^{182}\text{W}/^{184}\text{W}$ ,  $^{183}\text{W}/^{184}\text{W}$ , and  $^{186}\text{W}/^{184}\text{W}$  from Jacobsen (2005).  $^{179}\text{Hf}/^{180}\text{Hf}$  and  $^{180}\text{Hf}/^{184}\text{W}$  from Lodders (2010).

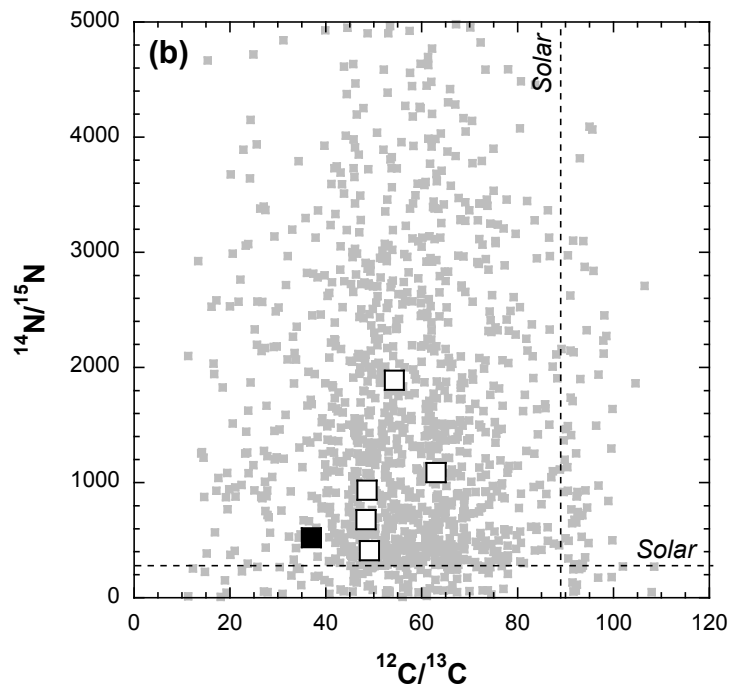
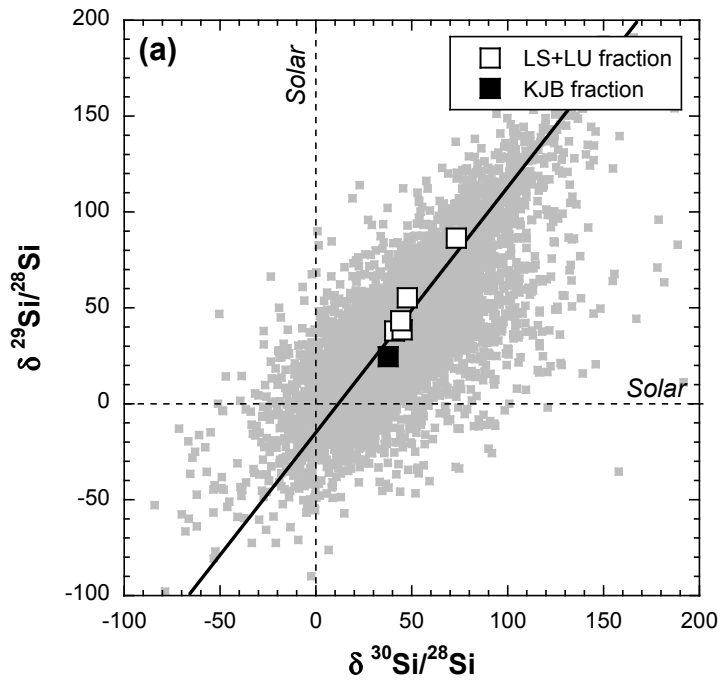
<sup>b</sup>  $\delta^i\text{W}/^{184}\text{W}$  (‰) =  $[(^i\text{W}/^{184}\text{W})_{\text{measured}} / (^i\text{W}/^{184}\text{W})_{\text{solar}} - 1] \times 10^3$ .

<sup>c</sup>  $\delta^{179}\text{Hf}/^{180}\text{Hf}$  (‰) =  $[(^{179}\text{Hf}/^{180}\text{Hf})_{\text{measured}} / (^{179}\text{Hf}/^{180}\text{Hf})_{\text{solar}} - 1] \times 10^3$ .

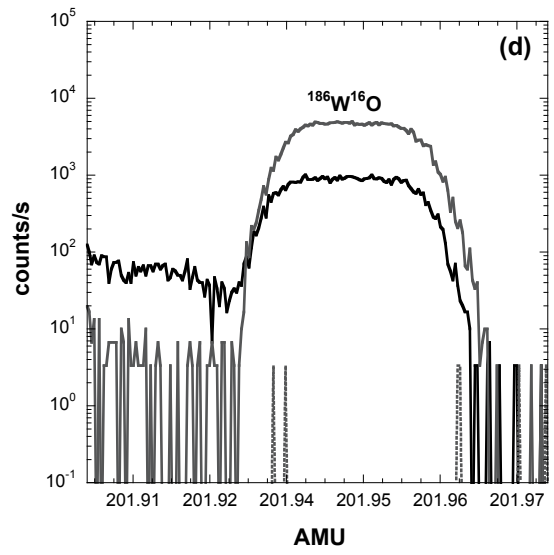
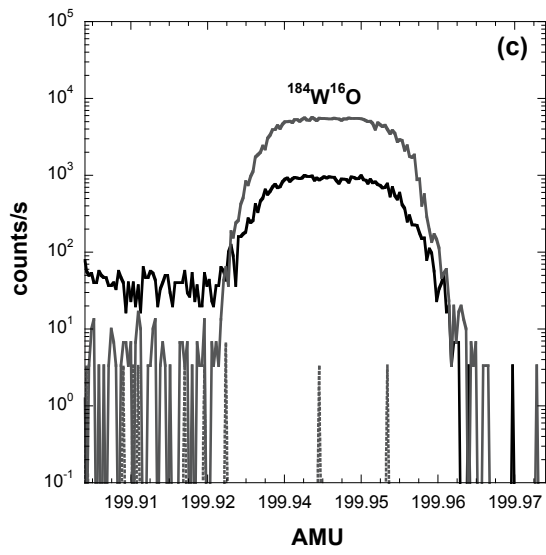
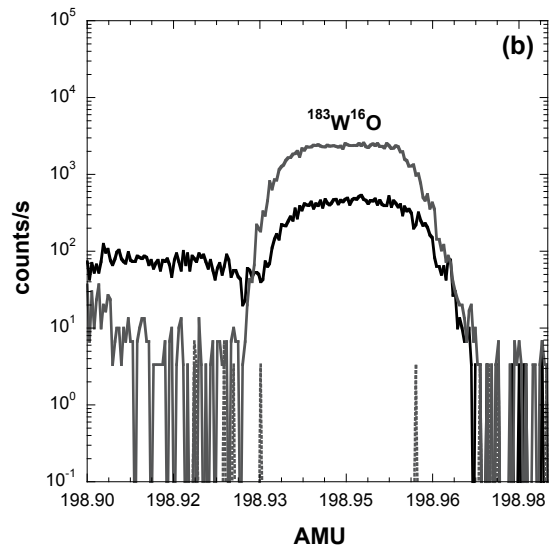
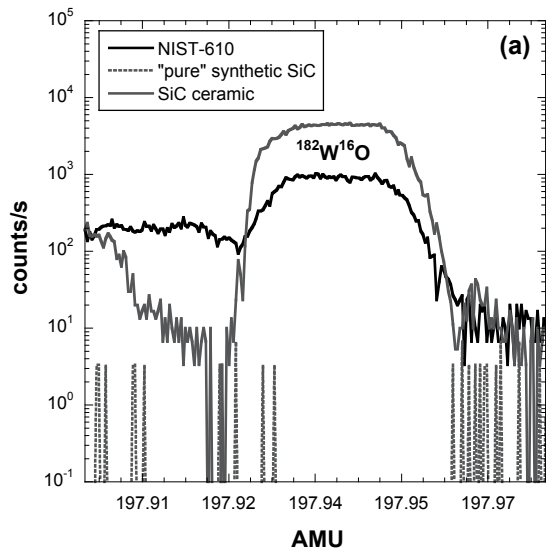
<sup>d</sup> corrected with relative sensitivity factor determined on the SiC ceramic.

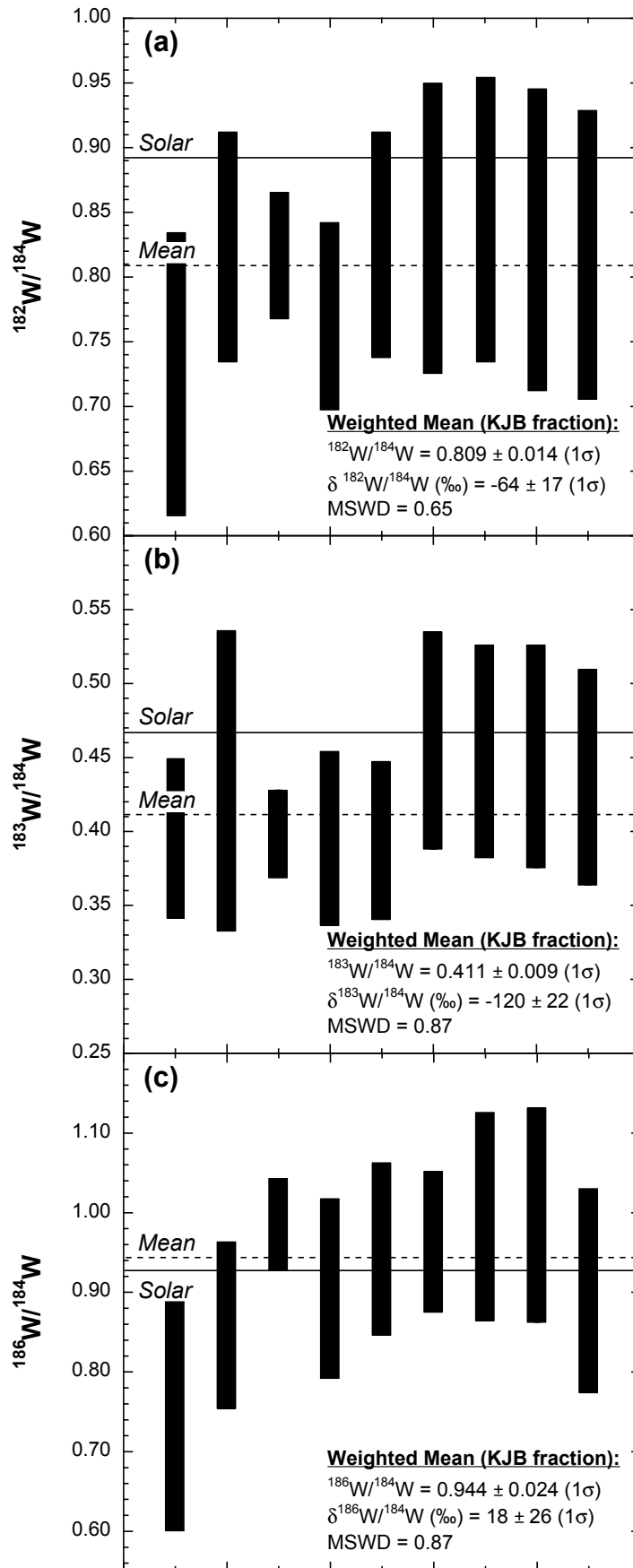
n.a. = not analysed; b.d.l. = below detection limit.

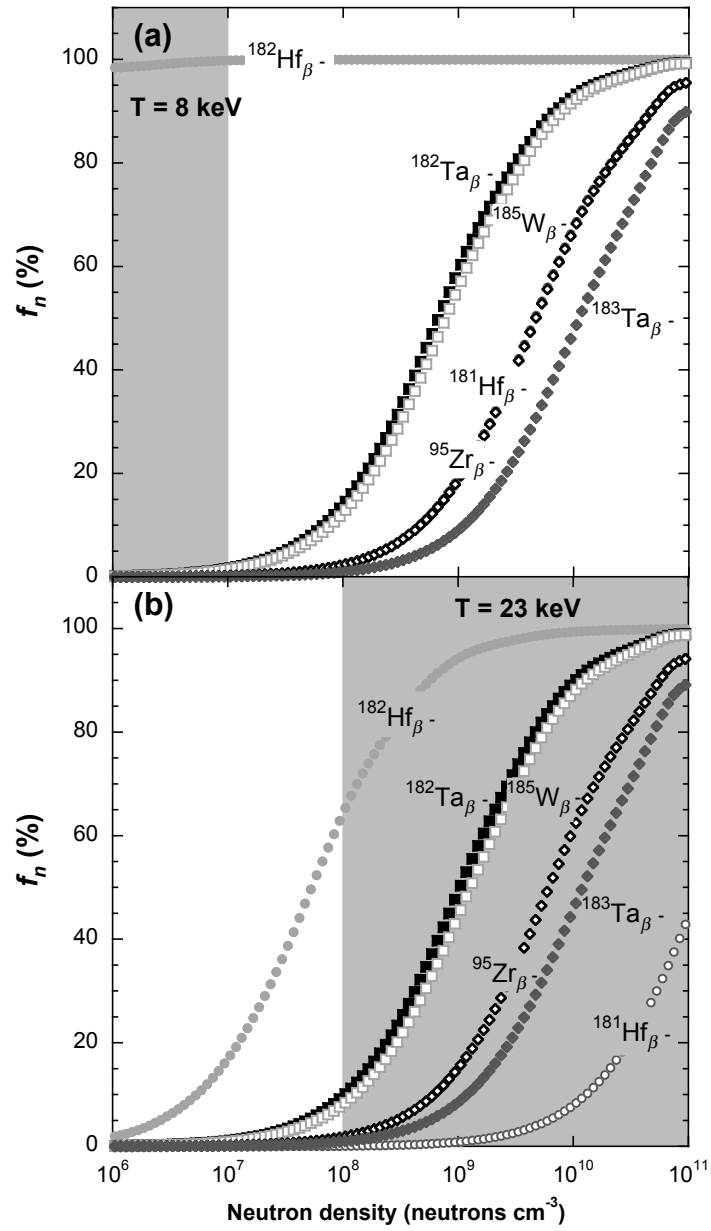




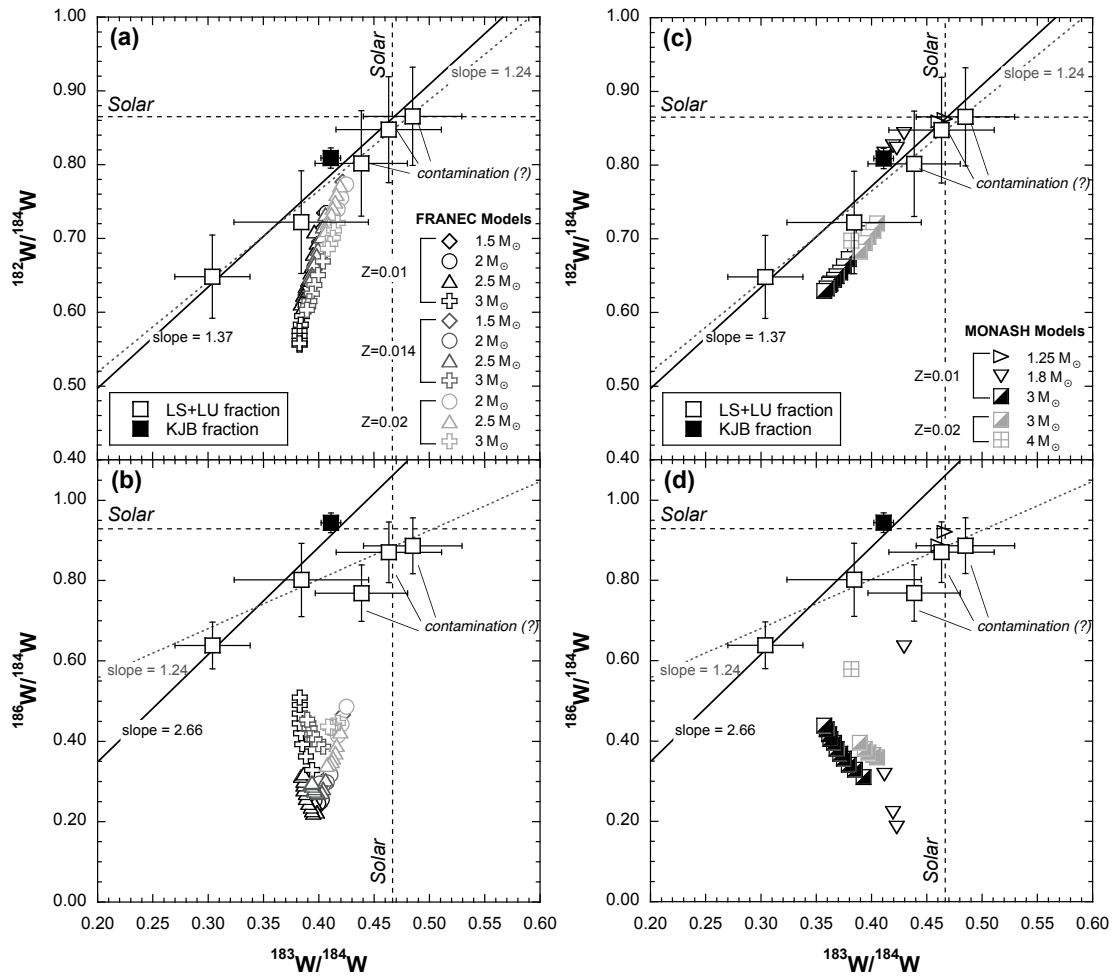
f2.eps



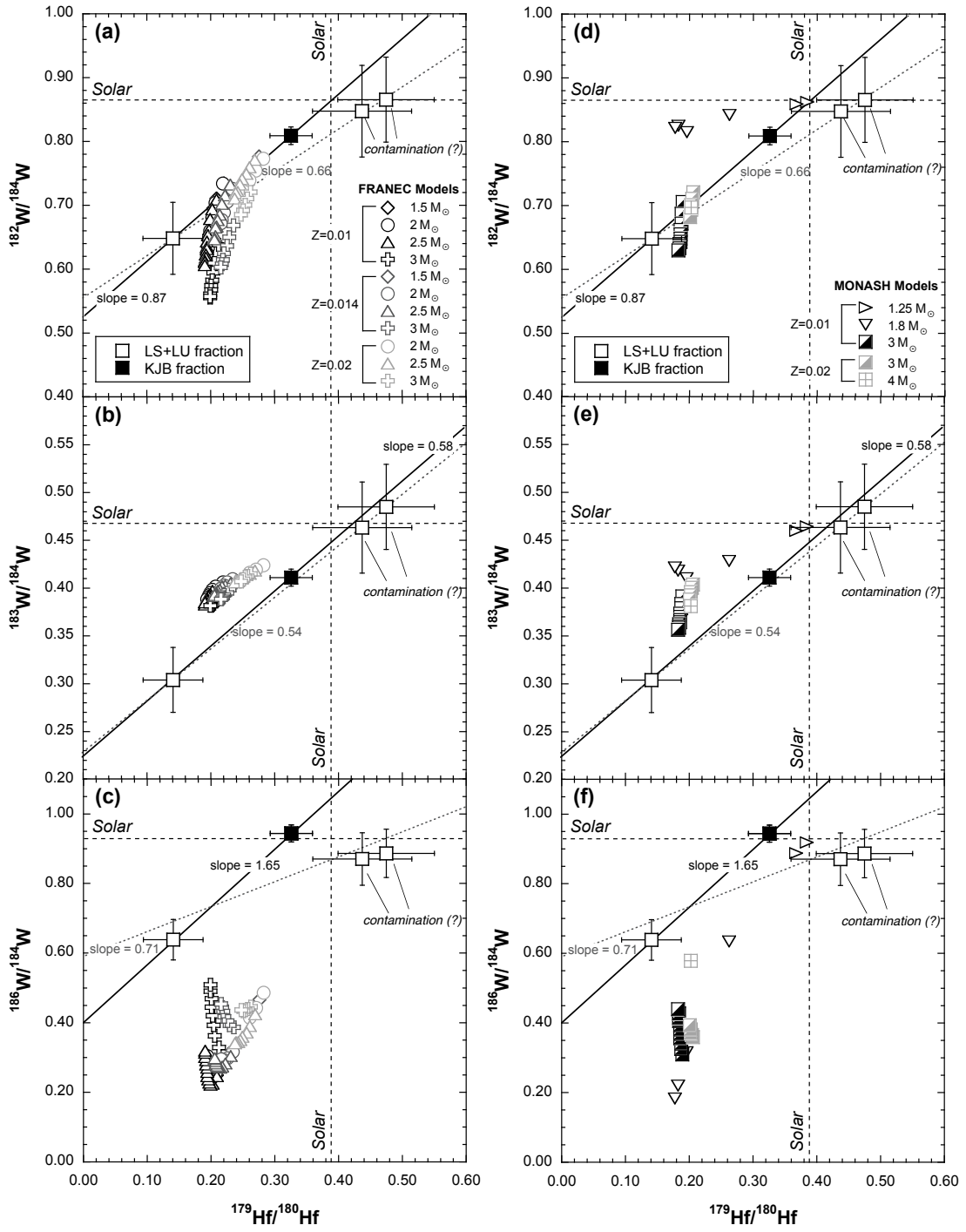




f5.eps



f6.eps



f7.eps